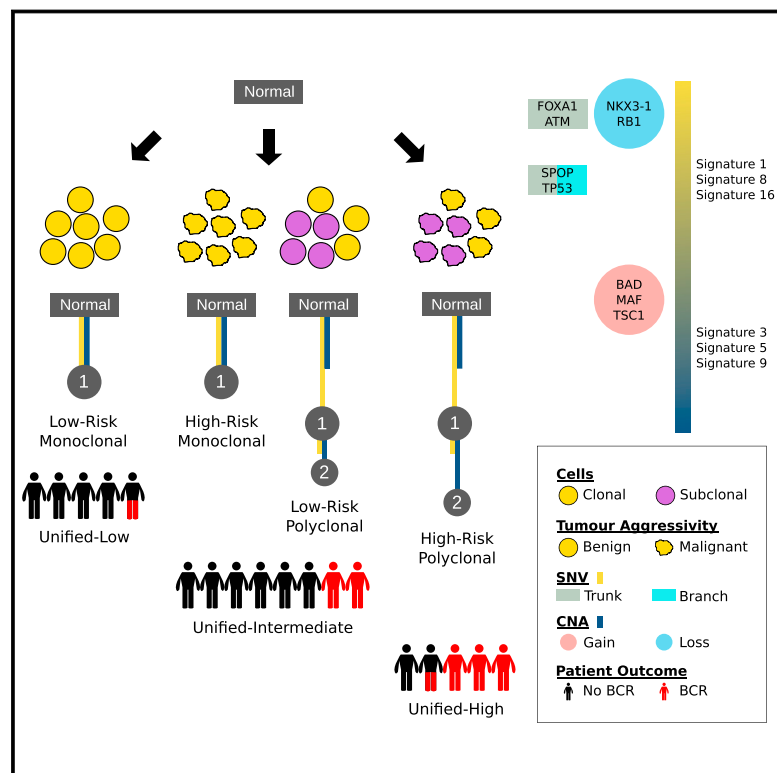# The Evolutionary Landscape of Localized Prostate Cancers Drives Clinical Aggression

Graphical Abstract

Authors

Shadrielle Melijah G. Espiritu, Lydia Y. Liu, Yulia Rubanova, ..., Quaid D. Morris, Robert G. Bristow, Paul C. Boutros

Correspondence

quaid.morris@utoronto.ca (Q.D.M.), robert.bristow@manchester.ac.uk (R.G.B.), paul.boutros@oicr.on.ca (P.C.B.)

In Brief

Tumors evolve during their natural life history. We studied the evolution of newly diagnosed prostate tumors and identified specific genes mutated early or late in a tumor's life history. Considering subclonality improved predictions of disease aggressivity, identifying those patients who might be good candidates for receiving less treatment.

Highlights

- The phylogenies of 293 localized prostate cancers were reconstructed

- Multiple subclones were detected in 59% of patients

- Specific genes are selectively mutated early or late in tumor evolution

- Subclonal architecture adds prognostic ability to previously developed biomarkers

CellPress

Resource

Cell

The Evolutionary Landscape
of Localized Prostate Cancers
Drives Clinical Aggression

Shadrielle Melijah G. Espiritu,[1,10] Lydia Y. Liu,[1,10] Yulia Rubanova,[2,3,10] Vinayak Bhandari,[1,4,10] Erle M. Holgersen,[1] Lesia M. Szyca,[1] Natalie S. Fox,[1,4] Melvin L.K. Chua,[5] Takafumi N. Yamaguchi,[1] Lawrence E. Heisler,[1] Julie Livingstone,[1] Jeff Wintersinger,[2,3] Fouad Yousif,[1] Emilie Lalonde,[1,4] Alexandre Rouette,[1] Adriana Salcedo,[1,4] Kathleen E. Houlahan,[1,4] Constance H. Li,[1,4] Vincent Huang,[1] Michael Fraser,[1,5] Theodorus van der Kwast,[6] Quaid D. Morris,[2,3,8,9,11,*] Robert G. Bristow,[4,5,11,*] and Paul C. Boutros[1,4,7,11,12,*]

[1]Informatics and Biocomputing Program, Ontario Institute for Cancer Research, Toronto, ON M5G 1L7, Canada
[2]Department of Computer Science, University of Toronto, Toronto, ON M5S 3G4, Canada
[3]Donnelly Centre for Cellular and Biomolecular Research, Toronto, ON M5S 3E1, Canada
[4]Department of Medical Biophysics, University of Toronto, Toronto, ON M5G 1L7, Canada
[5]Princess Margaret Cancer Centre, University Health Network, Toronto, ON M5G 2M9, Canada
[6]Department of Pathology and Laboratory Medicine, Toronto General Hospital/University Health Network, Toronto, ON M5S 1A1, Canada
[7]Department of Pharmacology and Toxicology, University of Toronto, Toronto, ON M5S 1A8, Canada
[8]Department of Molecular Genetics, University of Toronto, Toronto, ON M5S 1A8, Canada
[9]Vector Institute for Artificial Intelligence, Toronto, ON M5G 1M1, Canada
[10]These authors contributed equally
[11]Senior Author
[12]Lead Contact
*Correspondence: quaid.morris@utoronto.ca (Q.D.M.), robert.bristow@manchester.ac.uk (R.G.B.), paul.boutros@oicr.on.ca (P.C.B.)
https://doi.org/10.1016/j.cell.2018.03.029

SUMMARY

The majority of newly diagnosed prostate cancers are slow growing, with a long natural life history. Yet a subset can metastasize with lethal consequences. We reconstructed the phylogenies of 293 localized prostate tumors linked to clinical outcome data. Multiple subclones were detected in 59% of patients, and specific subclonal architectures associate with adverse clinicopathological features. Early tumor development is characterized by point mutations and deletions followed by later subclonal amplifications and changes in trinucleotide mutational signatures. Specific genes are selectively mutated prior to or following subclonal diversification, including *MTOR*, *NKX3-1*, and *RB1*. Patients with low-risk monoclonal tumors rarely relapse after primary therapy (7%), while those with high-risk polyclonal tumors frequently do (61%). The presence of multiple subclones in an index biopsy may be necessary, but not sufficient, for relapse of localized prostate cancer, suggesting that evolution-aware biomarkers should be studied in prospective studies of low-risk tumors suitable for active surveillance.

INTRODUCTION

Prostate cancer remains the most common non-skin malignancy in men. It is characterized by a long life history that leads to extensive intra-tumoral heterogeneity and subclones with wide genetic divergence at initial diagnosis (Boutros et al., 2015; Cancer Genome Atlas Research Network, 2015; Cooper et al., 2015; Fraser et al., 2017). Prostate cancer is curable when localized. Nevertheless, patients that harbor occult metastatic disease or have aggressive tumors with poor clinical outcome have genomic architectures comprising few recurrent mutations, specific somatic copy number aberrations and differential epigenetics (Fraser et al., 2017). There is some preliminary evidence, from small multi-region sequencing studies, that tumors that have escaped the gland show clonal adaption (Gundem et al., 2015). However, it remains unclear how tumors evolve prior to initial diagnosis and therapy. For example, while tumors initiated in the presence of germline *BRCA2* mutations harbor a unique mutational profile, it is unclear if other germline alleles influence tumor development (Taylor et al., 2017). It is natural to hypothesize that more genetically diverse tumors will have worse outcomes, but the clinical consequences of subclonal architecture and its impact on biomarkers remain unclear (Zhang et al., 2014).

Tumorigenesis proceeds through a sequential series of mutational events, some incremental and others catastrophic (Notta et al., 2016; Stephens et al., 2011; Vogelstein et al., 1988). Some of these selection and adaption events confer a selective growth advantage by overcoming micro-environmental and genetic selective pressures including the presence of intra-tumoral hypoxia and escaping telomere crisis. Spatio-genomic studies that have sequenced multiple regions of a single tumor have suggested that this process leads to most solid tumors being comprised of multiple clones (Gerlinger et al., 2012; McPherson et al., 2016; Nik-Zainal et al., 2012). Clones can harbor mutations common to all tumor cells (i.e., clonal or trunk
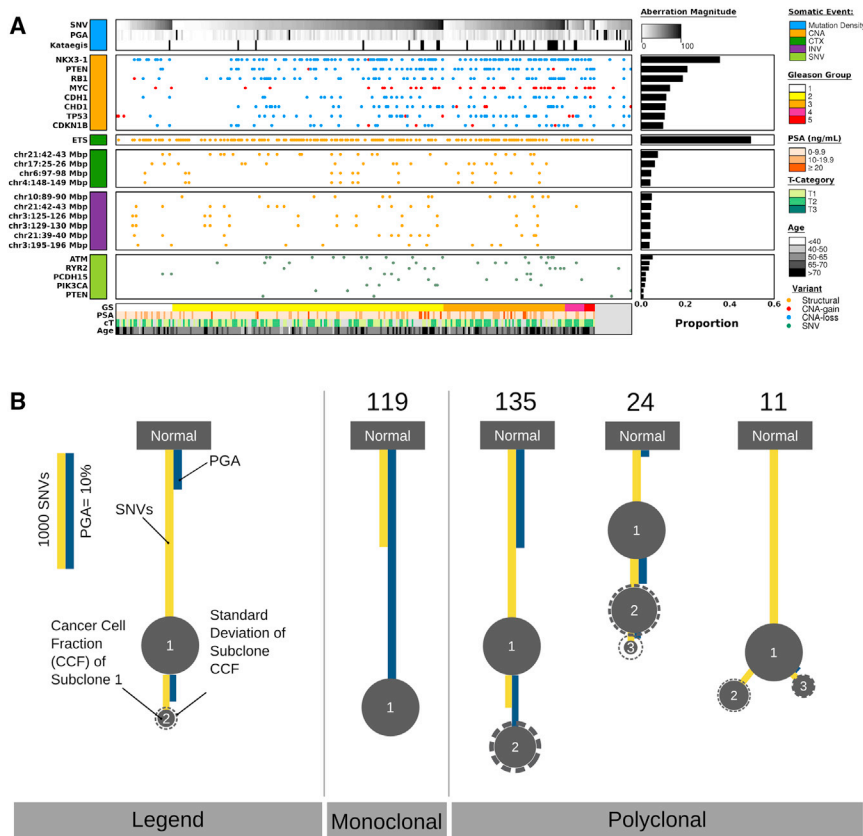
Figure 1. Subclonal Mutational Architecture of Localized Prostate Cancer

(A) The landscape of localized prostate cancer is shown for all 293 samples in the study. Data for mutational burden, CNAs, fusions, translocations, inversions, and SNVs are shown along with clinical information. Barplots on the right indicate the frequency of each event in the cohort.

(B) The diversity and the frequency in architecture of prostate cancer evolution are summarized. Tumors are divided into two groups: *monoclonal* with only one clonal population and *polyclonal* with at least one subclonal population. Mutational density is represented by the edge lengths: numbers of SNVs (yellow) and CNAs (as PGA, blue). Cancer cell fraction is given as the node diameter for each subclone, and dashed circles show one standard deviation of the subclone CCF across all tumors with identical trees. Representative trees are shown (see the STAR Methods). See also Figure S1, Table S1, and Data S1.

RESULTS

The Subclonal Architecture of Localized Prostate Cancer

To understand the subclonal architecture of localized prostate tumors, we studied 293 tumors from patients diagnosed with localized prostate cancer (Table S1). All tumors were treatment naive at the time of sampling, and 97% of the cohort was intermediate-risk by NCCN-criteria. Patients were treated with either surgery (radical prostatectomy) or image-guided external beam radiotherapy, and samples from the index lesion and paired normal (blood) samples were whole-genome sequenced (WGS). In addition to the 200 tumors we analyzed previously (Fraser et al., 2017), we analyzed an additional 93 tumor/normal whole-genome pairs (coverage = 74x ± 23x; number of single nucleotide variants (SNVs) = 609 ± 475; number of CNAs = 31 ± 27; mean ± SD; Figure 1A). For each patient, we reconstructed their tumor's subclonal profile by identifying somatic SNVs and subclonal copy-number aberrations (CNAs) and then integrating these on evolutionary trees (Figures S1A–S1C; Data S1). To verify the robustness of our subclonal CNA predictions, we contrasted them with reconstructions made by two alternative tools (Figure S1D; Table S1) and different mutation-calling pipelines (Figures S1L–S1O). We further validated our methodology in a transplantable cell-line model system (Figures S1H–S1K) and confirmed that subclonal reconstructions were not biased by sequencing site (Figure S1E) nor by sequencing coverage (Figures S1F and S1G). Of these 293 tumors, 41% had only clonal mutations (termed *monoclonal* tumors) detectable at our sequencing depth in the index lesion (Figure 1B; Table S1). The remaining 59% showed evidence of multiple tumor populations originating from a single ancestral clone (termed *polyclonal*). Of the polyclonal tumors, the majority (135/174) were biclonal, with only two populations being detected at the sensitivity of our sequencing depth and analytical
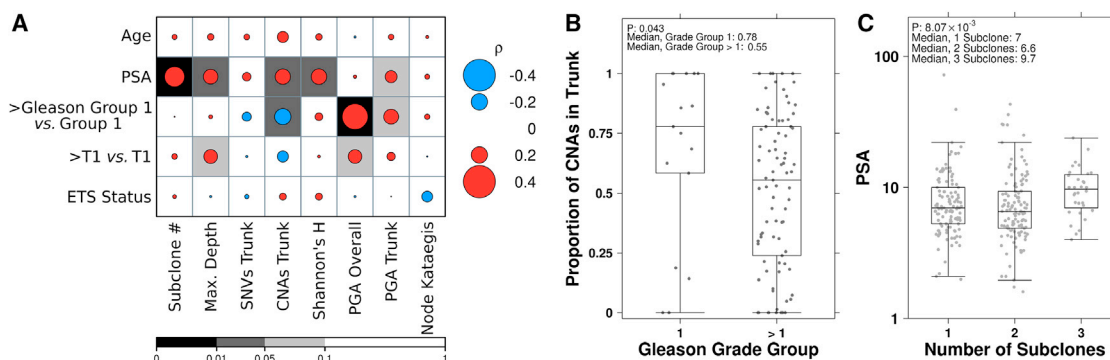
mutations), and mutations specific to one evolutionary branch of the tumor (i.e., subclonal or branch mutations). Because only small numbers of patients have received spatio-genomic profiling to date, the molecular origins and clinical consequences of tumor subclonality remain unclear. Previous studies of prostate cancer clonality using spatial sampling together comprise fewer than 20 patients, most with incurable metastatic disease selected by castrate resistance; no studies have systematically addressed subclonality in potentially curable tumors.

To address these issues and to explicitly evaluate the effects of tumor subclonality on the risk of relapse after initial definitive treatment, we reconstructed the subclonal architectures of 293 localized prostate tumors. We identified multiple cancer cell populations in 59% of specimens. Tumors are initially driven by clonal accumulation of point-mutations and genomic deletions, but after branching copy number gains become more common. Mutational stresses change temporally over the course of disease progression, with frequent changes in the pattern of trinucleotide signatures. Most prostate cancer driver mutations are clonal, but a subset preferentially occurs subclonally. Critically, prostate cancer clonality has clear clinical utility: patients with monoclonal tumors have extremely low rates of relapse. Our findings show that existing prognostic biomarkers can be confounded by subclonality, but when used strategically to enhance biomarker development, more accurate and personalized tests can be developed for intensification/deintensification of treatment for curable cancers.

Figure 2. Clinical Correlates of Phylogenetic Features

(A) The correlation between clinical variables and tumorigenesis is explored using Spearman's ρ. The background indicates the p value of the correlation, while dot size and color gives the magnitude and direction of the correlation.

(B) Tumors in Gleason grade group >1 had a lower proportion of CNAs in the trunk compared to Gleason grade 1 tumors (Mann-Whitney U test).

(C) Further, tumors with more than two subclones have higher serum abundances of PSA before treatment (Mann-Whitney U test).

See also Figure S2 and Table S2.

pipelines, while three populations were detected in 35 tumors. The remaining tumors showed characteristics consistent with being polytumors, suggestive of patients with multiple independent primary tumors, as observed in multi-region sequencing studies (Boutros et al., 2015; Cooper et al., 2015). However, reconstruction of these is challenging, and we therefore exclude these subclonal reconstructions in our analysis to remain conservative. Both monoclonal and polyclonal tumors appear to have evolved from a single ancestral cell, but the latter are distinguished by localized subclonal diversification since transformation of this founder cell. The bulk of analyses thus proceeded on a cohort of 289 consistently analyzed and subclonally reconstructed tumors (Data S1).

To assess whether these tumor phylogenies were associated with clinical characteristics, we tested their association with the prognostic variables of prostate-specific antigen (PSA), tumor grade (Gleason groups), and T-category, as well as age and E26 transformation-specific (ETS) fusion status. As a positive control (Lalonde et al., 2014), tumors with elevated Gleason groups showed elevated proportions of the genome copy-number altered (PGA; $p = 4.27 \times 10^{-2}$; Mann-Whitney U test; Figures 2A, 2B, S2A, and S2B; Table S2). Interestingly, tumors with an increased number of subclones have higher serum abundances of PSA prior to treatment (8.07×10^{-3}; Kruskal-Wallis test; Figure 2C). These data suggest that clonality is a separate entity to current prognostic factors.

Mutational Timing and Mutational Processes

Next, we sought to quantify the mutational processes underlying prostate tumorigenesis, and how these change over the course of tumor evolution. We first compared the types of mutations present in the trunk of tumors to those that occur in their branches. Most somatic point mutations occur in a tumor's trunk (75.4% ± 4.0% of SNVs); by contrast, CNAs were equally split between the trunk and its branches, with an average of 54.5% ± 5.4% of PGA occurring in the trunk ($p = 1.33 \times 10^{-5}$; Mann-Whitney U test; Figure 3A). CNAs occurring early in tumor evolution were strongly biased toward

deletions, with 84.0% ± 4.0% of all losses occurring in the trunk, compared to 63.3% ± 6.2% of gains ($p = 7.84 \times 10^{-9}$; Mann-Whitney U-test; Figure S2C). Trunk CNAs were larger than branch CNAs (11.5 Mbp versus 6.15 Mbp; $p < 2.20 \times 10^{-50}$; Mann-Whitney U test; Figure S2D). Thus the initial evolution of prostate cancer involves accumulation of SNVs (likely passenger mutations) and deletions, while later clonal divergence involves arm-length and focal gains.

To assess the mutational processes driving this early accumulation of somatic SNVs, we quantified the contribution of different trinucleotide mutation signatures (Alexandrov et al., 2013). For each patient, we sorted SNVs by their cancer cell fractions (CCFs) corrected by copy number, divided them into bins of 400 and estimated mutational timing in a sliding window manner (see the STAR Methods). Mutational signatures were fit at each bin using a multinomial mixture model, focusing on the six signatures most strongly present in our cohort (Figure S3A), which include the aging (S1) and homologous recombination deficiency signatures (S3) (Alexandrov et al., 2013). About half of all patients (132/289) exhibited detectable changes in signature exposure over the course of their tumor evolution, providing a lower-bound on changes in the mutational pressures at play (Figure 3B). We separated patients into six distinct sub-groups based on the pattern of change (Figures 3B and S3B; Table S1) and identified groups of patients showing large switches in signature profiles over time, including decreases in the aging signature (signature S1) and increases in the homologous recombination deficiency signature S3 (Figure 3C; Table S3; Data S1). In exploratory analyses, these changes were not correlated to specific clinico-pathologic variables, although additional larger cohorts will be needed to investigate this question. Decrease in the activity of the aging signature S1 may reflect an elevation in other mutagenic stresses over time rather than an actual decrease in the specific functioning of that mutagenic process. By contrast, increase in the activity of S3 is preferentially associated with CNA loss of *BRCA2* (odds ratio [OR] 3.37, 95% confidence interval 0.85–11.57; p = 0.043; Fisher's exact test). This finding is concordant with increased *BRCA*
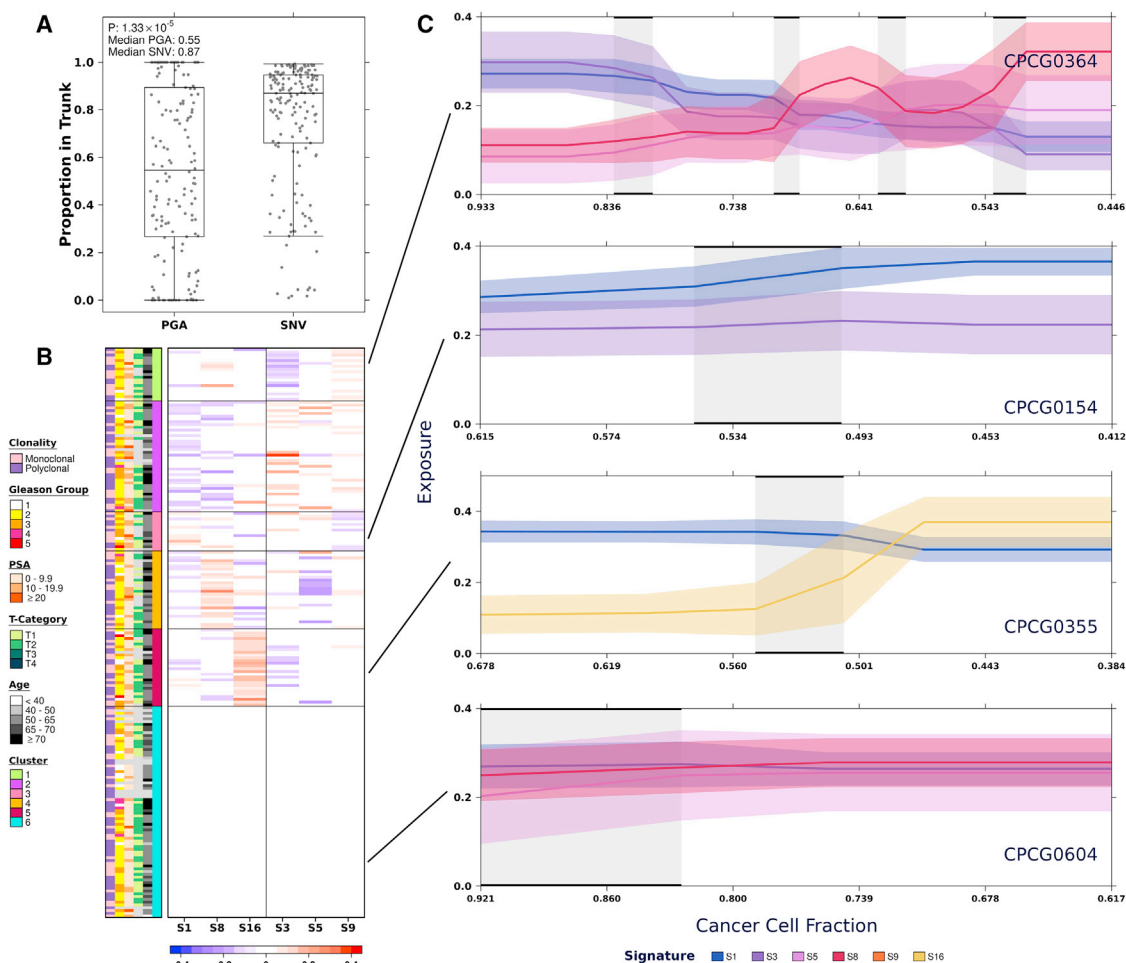
Figure 3. Evolution of Mutational Processes in Prostate Cancer

(A) The acquisition of mutations during tumor evolution is differentiated. Differences in the proportion of SNVs and PGA emerging from trunk are tested with a Mann-Whitney U test.

(B) The six most prevalent signatures in our cohort and their exposure changes from the first time point to the last are displayed. Signatures are clustered into six groups, and samples are ordered by their signature changes.

(C) Exemplars with varying exposures are shown. Uncertainty was evaluated by bootstrapping sets of mutations and re-computing exposure estimates 30 times. The SD of the exposures at each time point is shown as the shaded area around the trajectory. Signatures whose error bars overlap at all time points are deemed to have no change. Signature changepoints are highlighted using black bars with a shaded background.

See also Figure S3 and Table S3.

loss and DNA repair gene dysfunction in metastatic castrate-resistant prostate tumors (Robinson et al., 2015).

Molecular Hallmarks of Subclonality

We hypothesized that the different mutational processes present in the trunk and branch of prostate tumors would reflect distinct sets of driver mutations occurring in these two different phases of tumor evolution. We considered all genes recurrently affected by functional somatic SNVs (genes with nonsynonymous, stop-loss, stop-gain and splice-site SNVs in at least 2% of patients, or previously identified as recurrently mutated by Fraser et al. [2017]), independent of driver significance (Tables S1 and S4). Some SNVs were strictly clonal (i.e., found in tumor trunks), including the well-known prostate cancer genes *FOXA1* and *ATM* (Figures 4 and S4A; Table S4). By contrast, others were mutated both clonally and subclonally (e.g., *TP53* and *SPOP*). We attempted to identify non-coding SNVs with trunk versus branch bias, but were underpowered, given the low recurrence rate of non-coding SNVs (Figure S4B; Table S4).

As prostate cancer is a C-class tumor (Fraser et al., 2017), we focused on the evolution of CNA profiles. We identified specific CNAs strongly enriched in the trunk of the tumor (Tables S1 and S5), including the hallmark *NKX3-1* deletion found in 126/289 patients and occurring in the trunk 89.7% of the time (q = 4.55 × 10^{-10}; Pearson's χ^2 test). Other genes strongly enriched for clonal deletion included loss of *RB1* (87% clonal; q = 2.40 × 10^{-4}; Pearson's χ^2 test) and a locus on chromosome 16 containing the tumor-suppressor *MAF* (66/75 in trunk;
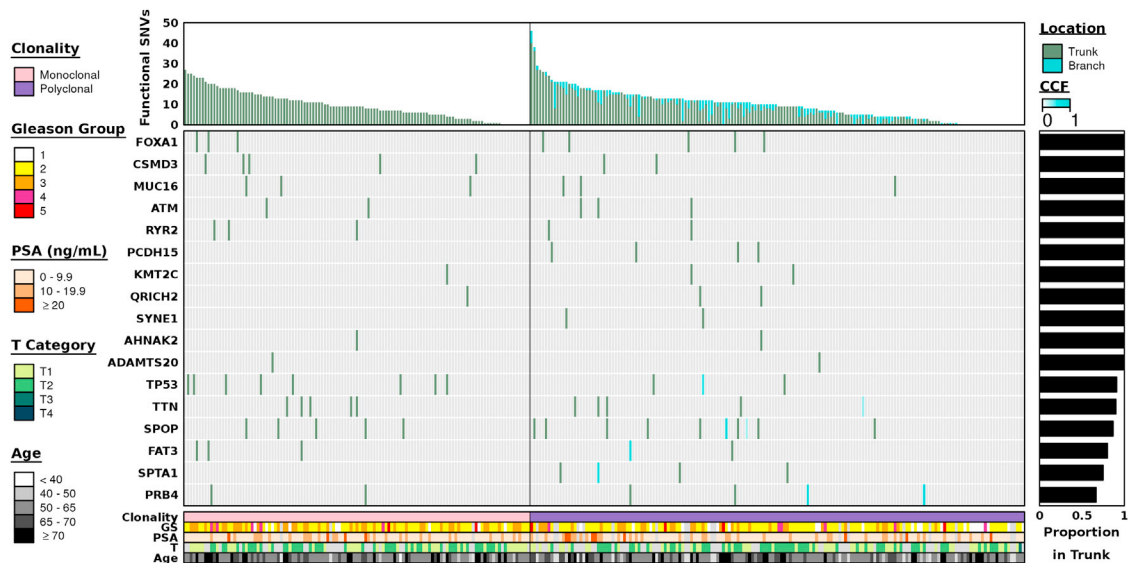
Figure 4. Evolution of Recurrent SNV Mutations
The timing of occurrence of recurrent SNV mutations in prostate cancer is evaluated. Mutations are classified as trunk or branch according to their time of occurrence. Trunk mutations distinguish all cancerous cells from the normal population, while branch mutations develop after clonal establishment. Patients are ordered by total number of functional mutations (i.e., missense and nonsense), while recurrent SNVs are sorted by proportion defined as trunk and overall frequency. The cancer cell fraction measures the proportion of the tumor population that harbors the mutation.
See also Figure S4 and Table S4.

$q = 4.06 \times 10^{-5}$; Pearson's χ^2 test), which is linked to ETS-rearranged tumors (Demichelis et al., 2009). Other genes were subject to recurrent subclonal CNAs, including mediators of cellular response and signaling (e.g., *MTOR*, *TP73*); regulators of growth and apoptosis (e.g., *BAD, VEGFB*); and other cancer driver genes (e.g., *CCND1, CCNE1, JUNB, TSC1, TSC2,* and *KEAP1*; Figure 5A; Tables S1 and S5). Several recurrent clonal tumor suppressor losses, including *RB1*, *APC*, and *CDKN1B*, resulted in clear changes in mRNA abundance in 127 patients with transcriptome profiling (Table S5). Pathway analysis revealed that genes in regions with CNAs showing biased evolutionary timing are enriched for regulation of death receptor transcription by TP53, apoptosis, and PI3K/AKT activation (Figure S5A; Table S5).

To better understand these evolutionarily biased CNAs, we used unsupervised clustering separately on trunk CNA profiles and on branch CNA profiles. Consensus clustering identified four trunk subtypes (*A*, *B*, *C*, and *D*) and three branch subtypes (*e*, *f*, and *g*; Figure 5A). Clonal and subclonal subtypes were not correlated with one another (Figure S5B). Both the trunk and branch subtypes reflected concomitant changes at multiple loci (Figures 5B and 5C). Branch subtype *e* was enriched in gains at chromosome ends, suggesting changes in telomeres that occur subclonally. Consistent with this, monoclonal tumors have ~500 bp longer telomeres than polyclonal tumors ($p = 4.74 \times 10^{-2}$; Mann-Whitney U test; Figure S5C). Telomere lengths varied within both clonal and subclonal CNA subtypes (Figures S5D and S5E). Branch subtype *e* replicates a CNA subtype identified in previous microarray analyses (Figures S5F–S5H). These patients have longer telomeres than the rest of the cohort (Figure S5I) and harbor gains of both telomerase

reverse transcriptase *(TERT)* and DNA methyltransferase 1 *(DNMT1*; Figures S5J and S5K) which both regulate telomere length (Gonzalo et al., 2006).

Clinical Relevance of Tumor Subclonality
Metastatic prostate tumors, which are incurable, harbor large numbers of spatially co-segregating subclones, with important implications for novel therapeutic approaches based on molecular phenotyping. We therefore assessed whether the subclonality of a localized (potentially curable) tumor reflects its relative aggressiveness in a 200-patient subset of the cohort where a median 8.85-year clinical follow-up was available. Patients whose tumor sample showed no evidence of multiple sub-populations showed significantly superior outcome to those whose tumors were polyclonal (HR = 2.64, 95% confidence interval [CI]: 1.36–5.15; $p = 4.22 \times 10^{-3}$; Wald test). As a prognostic biomarker, clonality compares favorably to the very best tissue-based prognostic tests available (Cuzick et al., 2011; Erho et al., 2013; Klein et al., 2014; Lalonde et al., 2014, 2016). Critically, these survival differences persist even after adjustment for the clinical prognostic factors pre-treatment PSA, clinical Gleason score, clinical T-category and PGA (Table S6).

To determine if subclonal mutations directly influence the accuracy of existing biomarkers, we considered two validated DNA-based prognostic tests: PGA (with an operating threshold of 7.49%) and a 100-locus genomic classifier (Lalonde et al., 2014). We first assessed how accurately microarray-based CNA assays, which predominate the literature, detect subclonal CNAs (Figure S6A). Arrays identified a large fraction of clonal CNAs detected by WGS (42.2% ± 6.1%), but did not identify most subclonal CNAs (10.6% ± 3.6%; $p = 1.17 \times 10^{-10}$;
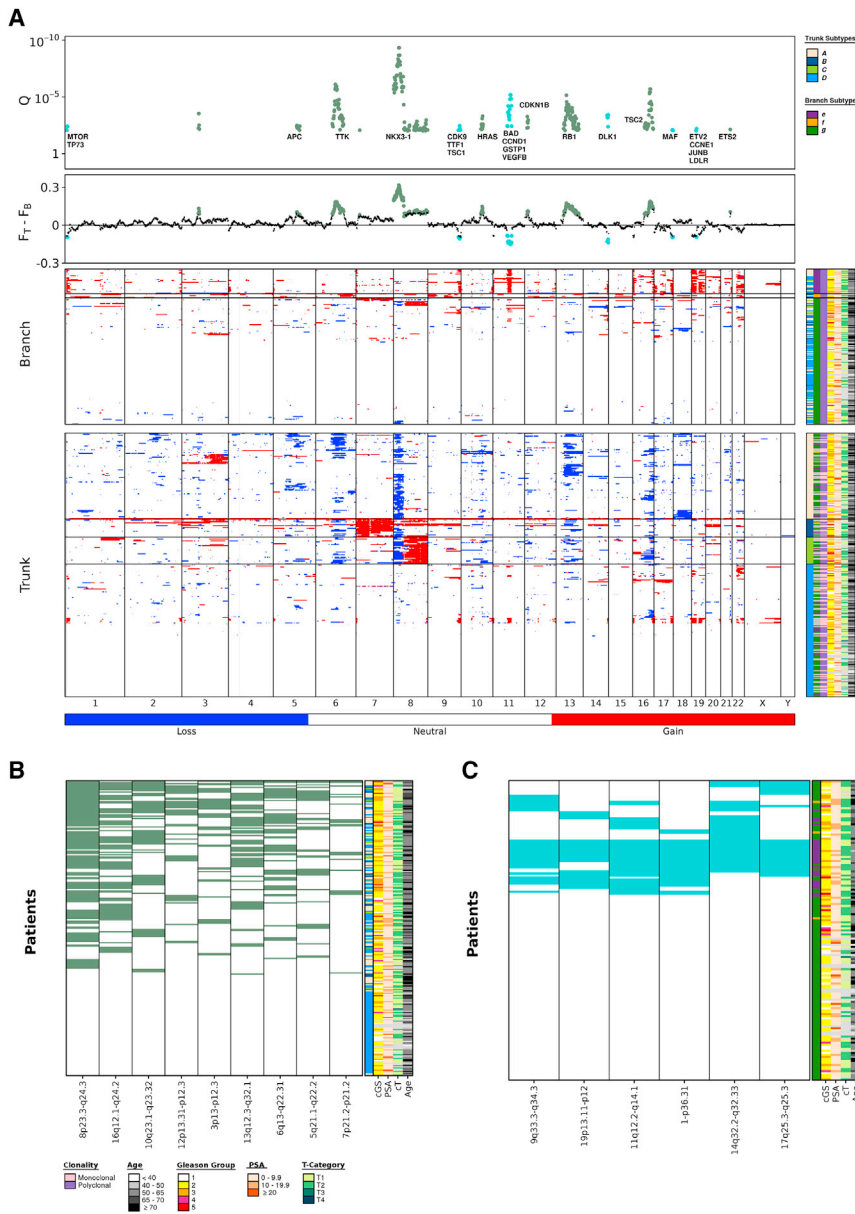
Figure 5. Evolution of Recurrent CNA Mutations

(A–C) The relative difference in CNA occurrence during the evolution of prostate cancer is assessed by subclonal reconstruction.

(A) CNA profiles of 289 prostate tumors split by CNA occurrence in trunk and branch. Red indicates gain; blue indicates loss; rows represent patients; and columns represent 1 Mbp genomic bins. Patients are clustered by their trunk and branch CNA profiles. The top two plots reflect trunk-branch differences in CNA frequency, showing the statistical significance (top plot, Q-value) and effect size (difference in frequency between trunk and branch, $F_{Trunk}-F_{Branch}$). Key altered genes (Pearson's χ^2 test, FDR adjustment) within these regions are labeled.

(B and C) The co-occurrence of trunk and branch biased loci, respectively.

See also Figure S5 and Table S5.

biomarker (Figure 6B). Similar results were seen using PGA (Figures S6J and S6K). Thus, our results suggest that low-risk monoclonal patients are highly unlikely to experience relapse after definitive local therapy, while polyclonal patients can be further divided based on genomic criteria into good and poor prognosis groups.

To evaluate the impact of subclonal populations on established prognostic biomarkers, we first focused on PGA. For each patient we considered what fraction of their biomarker risk-score was derived from CNAs present in the trunk of the tumor and what fraction was derived from subclonal CNAs present in the most aggressive clone. On average, patients derived 75.0% ± 4.4% of their risk from clonal CNAs and 25.0% ± 4.4% from branch CNAs (Figures 6B and S6G; Table S6). The PGA of monoclonal and polyclonal patients did not differ (p = 0.59; Mann-Whitney U test; Figures S6H and S6I). We identified 13% of patients as having clonal risk-score predictions indicating low-risk disease, but who harbored aggressive high-risk subclones that changed their risk stratification (Figures 6C and 6D). Similar results were obtained using a published 100-locus CNA-based prognostic signature, with 8.9% of patients harboring high-risk subclones on a background of low-risk trunks (Figures S6D–S6F; Table S6). Clonality not only characterizes tumors that are more likely to relapse after definitive local therapy but also those more likely to metastasize (Figure S7). Thus aggressive polyclonal tumors are characterized by elevated genomic instability and specific mutational profiles, and these findings advocate for the direct inclusion of tumor evolution biomarkers to improve delivery of precision cancer medicine.
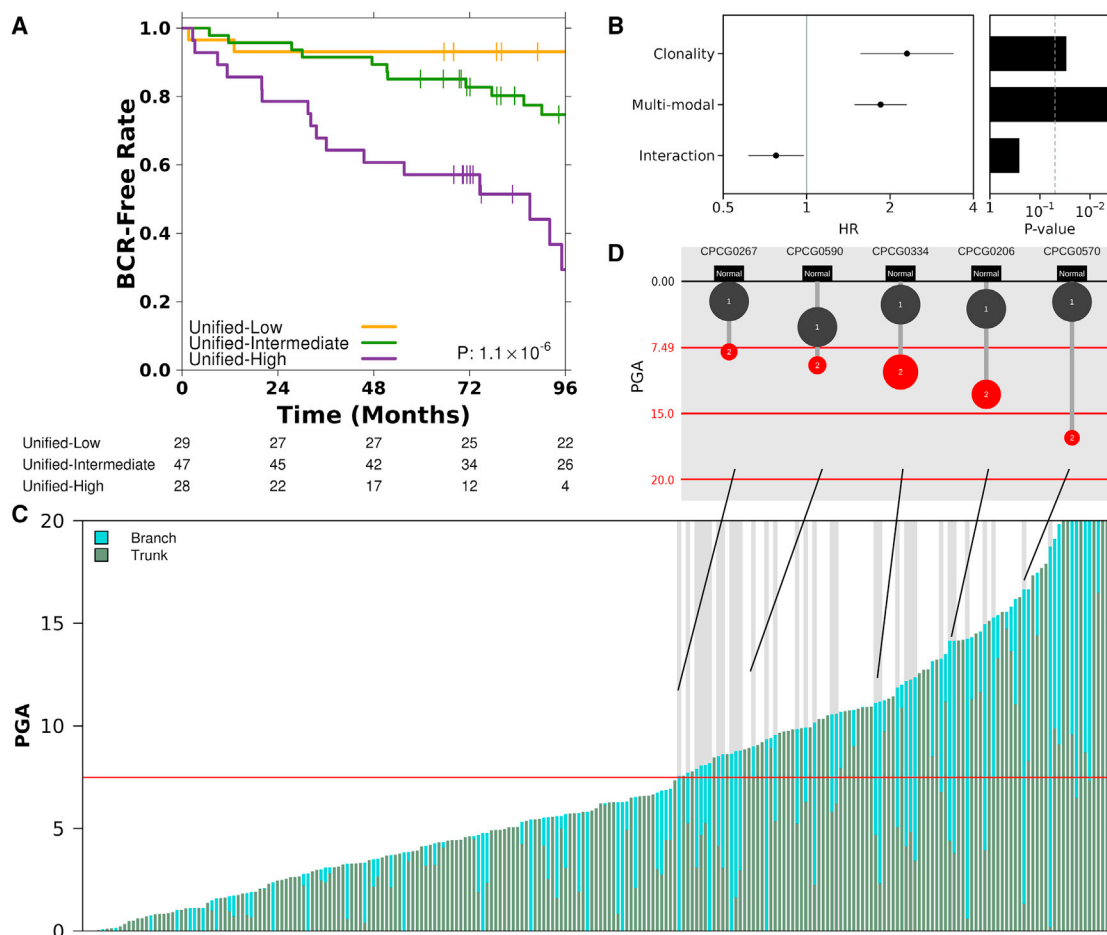
Mann-Whitney U test). We compared this finding on an independent dataset (Taylor et al., 2010) and found similar insensitivity (Figure S6B; Table S6). This lack of sensitivity suggests that false negatives in validated microarray-based tests may result from rare aggressive subclones that were not detected (Figure S6C).

Finally to establish if clonality could supplement existing genomic biomarkers developed on bulk samples, we stratified the patients using a multi-modal (CNA, SNV, SV, and methylation) biomarker scored on the bulk tumor sample (Fraser et al., 2017) integrated with clonality data to create a unified biomarker. This signature robustly stratified patients into groups with distinct prognoses (p = 1.10 × 10⁻⁶, log-rank test; Figure 6A). Importantly, clonality was additive with the multi-modal

Figure 6. Clinical Relevance of Subclonality

(A) Patient survival outcome stratified with a unified subclonally aware biomarker, which combines a previously developed multi-modal biomarker by Fraser et al. (2017) and tumor clonality. Univariate modeling was carried out using a log-rank test.

(B) Tumor clonality provides additive prognostic with the multi-modal biomarker in multivariable Cox proportional hazards modeling.

(C) Patients are ordered by their total risk as assessed by PGA. The red line divides the low-risk (PGA < 7.49%) from the high-risk (PGA ≥ 7.49%) patients. Bars with a gray background indicate patients who are considered low risk when only trunk mutations are considered but harbor high-risk clones detected by considering CNAs that occur in subclonal populations.

(D) Exemplars of these cases are shown. Red outlines the point at which the patient is classified as high risk.

See also Figure S6 and Table S6.

DISCUSSION

Multi-region sequencing has revealed key aspects of tumor evolution from small numbers of patients. We evaluated a large cohort of localized prostate tumors to understand the population characteristics of their subclonal evolution. Despite modest depth sequencing of a single spatial region, we are able to show that a subset of driver mutations occurs late in prostate tumor development, and these aggregate into subtypes that reflect divergent and changing mutagenic stresses on tumors (de Bruin et al., 2014). These observations support the hypothesis that more genetically diverse tumors have inherently worse outcome, perhaps due to an increased ability to adapt to local or systemic (e.g., androgen deprivation therapy) therapeutic intervention. Importantly, it appears from multi-region

sequencing studies that essentially all prostate tumors have significant poly-clonality because of spatial segregation of distinct tumor populations (Boutros et al., 2015; Cooper et al., 2015), but we show here that a subset of these show elevated local subclonal diversification. These tumors are largely biclonal, at least at the current sequencing depth and analytical sensitivity; deeper sequencing coverage, improved computational methods or single-cell sequencing may uncover deeper subclonal structure. Localized subclonal diversification is directly associated with the aggressiveness of disease: patients with only a single subclone in the index lesion tumor have remarkably good outcome. Indeed, existing biomarkers of patient survival are only effective in patients with polyclonal tumors, suggesting that polyclonality is necessary, but not sufficient, for aggressive disease. It may be that localized clonal diversity increases the
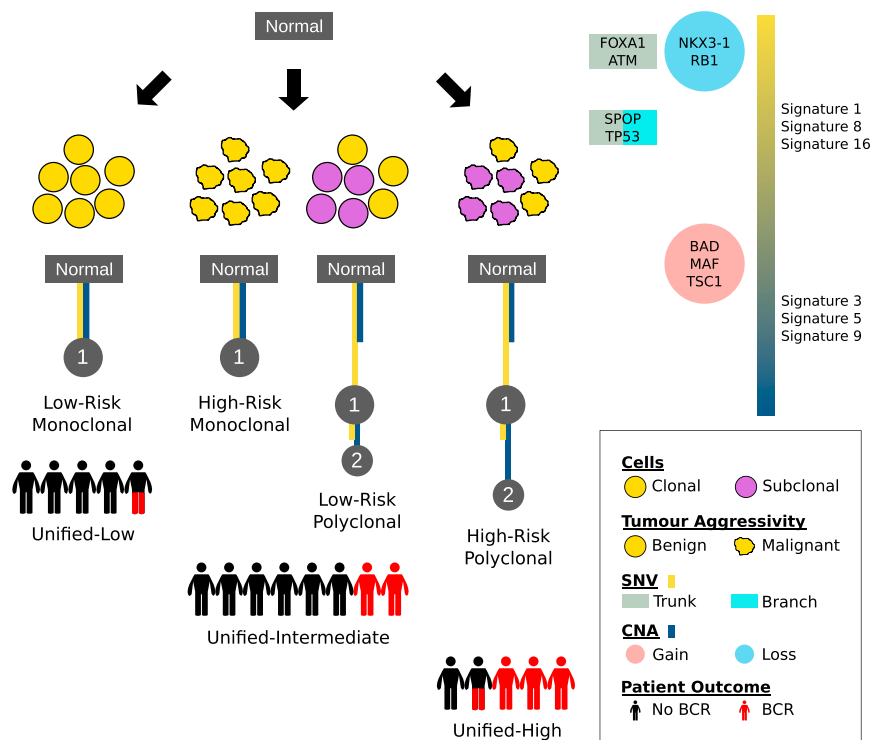
Figure 7. Evolutionary Trajectory Model for Prostate Cancer

An evolutionary model of prostate tumorigenesis. Early prostate cancer is largely characterized by the accumulation of SNVs in genes like *FOXA1* and *ATM*, along with loss of hallmark tumor suppressors, including *NKX3-1* and *RB1*. Initially, the aging signature (signature 1) predominates mutational processes, but over time additional driver SNVs accumulate, including *SPOP* and *TP53*, eventually leading to multiple subclones mixing in a single spatial location. This mostly linear tumor development in a spatially restricted area contrasts to the spatio-genomic heterogeneity of prostate cancer, and separates the monoclonal from polyclonal cancers. This sets the stage for subclonal driver amplifications in *MTOR*, *TSC1*, *TSC2*, *BAD*, *BID*, *BAK1*, and others. While driver SNVs become less common at this stage, the homologous recombination deficiency signature (signature 3) grows in intensity. Tumors can be stratified into low-, intermediate-, and high-risk groups by integrating subclonal architecture and biomarker features from Fraser et al. (2017), including *ATM* SNVs and *MYC* gains. Proportion of patients with a biochemical relapse is shown per class, with red indicating an event. Mutations are color-coded by spatial occurrence (trunk vs. branch) and CNA type (gain vs. loss). The right-hand bar shows the proportion of SNVs and CNAs throughout tumor development.

See also Figure S7.

probability that a clone capable of metastatic spread will arise, or that it reflects some inherent feature of the evolutionary adaptability of the tumor. Independent of the mechanism of this association, these data strongly support the use of WGS-based biomarkers to allow robust subclonal inference since microarray-based assays are prone to false-negative errors when small aggressive subclones are present.

Combined with previous studies, a picture of the life-history of aggressive prostate cancer is beginning to emerge. Tumors start with slow gradual accumulation of SNVs, punctuated by deletion of some tumor suppressors. In a subset of tumors, driver mutations or other phenomenon induce a switch to the rapid accumulation of copy number gains. These driver mutations lead to changes in the set of active mutational processes, particularly increased homologous recombination deficiency even in early localized disease (Robinson et al., 2015). Concomitant evolutionary branching create subclonal diversity, and a subset of these subclones survive primary, definitive therapy, either at the original site or as occult metastases. The surviving tumor subclones expand to form a network of related clones that colonize, compete, and collaborate across multiple metastatic sites (Gundem et al., 2015). However, this broad life history hides large inter-tumoral differences in driver genes, mutagenic processes, and clinical aggressivity. Moving forward, it will be key to develop very large, clinically well-annotated patient cohorts that will allow mechanistic insight into the specific clinical implications of different subclonal driver architectures and mutational processes.

Overall, this life history of prostate cancer implies that early identification of tumors with multiple subclones and aggressive

genomic and epigenomic features will improve cure rates through personalized therapy (Figure 7). These patients with highly aggressive tumors may benefit from adjuvant systemic treatment (e.g., androgen deprivation therapy) to prevent failure from occult metastatic disease. By contrast, our data provocatively suggest that patients with monoclonal tumors who are intermediate risk based on NCCN criteria could be studied for inclusion in trials of active surveillance.

STAR★METHODS

Detailed methods are provided in the online version of this paper and include the following:

- KEY RESOURCES TABLE
- CONTACT FOR REAGENT AND RESOURCE SHARING
- EXPERIMENTAL MODEL AND SUBJECT DETAILS
  - Patient Cohort
  - Transplantable Metastasis Model
- METHOD DETAILS
  - SNP Microarray Data Analysis
  - Whole-Genome Sequencing Data Analysis
  - Somatic Subclonal Copy Number Assessment
  - Phylogenetic Reconstruction of Tumors
  - Cell Line Validation
- QUANTIFICATION AND STATISTICAL ANALYSIS
  - Scoring Tree Structures
  - Classifying Mutations
  - Representative Tree Structures

- Subclonal Analysis of Recurrent Mutations
- Pathway Analysis
- Subclonal Analysis of Kataegis
- Trinucleotide Mutation Signatures
- Subclonal Tree Correlations
- Microarray Sensitivity
- Survival Analysis
- Scoring Biomarker Signatures
- Data Visualization and Reporting
● DATA AND SOFTWARE AVAILABILITY

SUPPLEMENTAL INFORMATION

Supplemental Information includes seven figures, six tables, and one data file and can be found with this article online at https://doi.org/10.1016/j.cell.2018.03.029.

AUTHOR CONTRIBUTIONS

Data Analyses: S.M.G.E., L.Y.L., Y.R., V.B., E.M.H., N.S.F., M.L.K.C., T.N.Y., L.E.H., J.L., J.W., F.Y., E.L., A.R., C.H.L., V.H., Q.D.M., and P.C.B. Data Visualization: S.M.G.E., L.Y.L., V.B., E.M.H., L.M.S., N.S.F., A.S., and K.E.H. Supervised Research: M.L.K.C., M.F., T.v.d.K., Q.D.M., R.G.B., and P.C.B. Initiated the Project: S.M.G.E., L.Y.L., Q.D.M., R.G.B., and P.C.B. Wrote the First Draft of the Manuscript: S.M.G.E., L.Y.L., V.B., E.M.H., and P.C.B. All authors approved the manuscript.

DECLARATION OF INTERESTS

A provisional patent has been filed by S.M.G.E., L.Y.L., R.G.B., and P.C.B. under patent number US62/473,875. The authors have no other competing interests to declare.

REFERENCES

Alexandrov, L.B., Nik-Zainal, S., Wedge, D.C., Aparicio, S.A.J.R., Behjati, S., Biankin, A.V., Bignell, G.R., Bolli, N., Borg, A., Børresen-Dale, A.-L., et al.; Australian Pancreatic Cancer Genome Initiative; ICGC Breast Cancer Consortium; ICGC MMML-Seq Consortium; ICGC PedBrain (2013). Signatures of mutational processes in human cancer. Nature 500, 415–421.

Baca, S.C., Prandi, D., Lawrence, M.S., Mosquera, J.M., Romanel, A., Drier, Y., Park, K., Kitabayashi, N., MacDonald, T.Y., Ghandi, M., et al. (2013). Punctuated evolution of prostate cancer genomes. Cell 153, 666–677.

Berger, M.F., Lawrence, M.S., Demichelis, F., Drier, Y., Cibulskis, K., Sivachenko, A.Y., Sboner, A., Esgueva, R., Pflueger, D., Sougnez, C., et al. (2011). The genomic complexity of primary human prostate cancer. Nature 470, 214–220.

Boutros, P.C., Fraser, M., Harding, N.J., de Borja, R., Trudel, D., Lalonde, E., Meng, A., Hennings-Yeomans, P.H., McPherson, A., Sabelnykova, V.Y., et al. (2015). Spatial genomic heterogeneity within localized, multifocal prostate cancer. Nat. Genet. 47, 736–745.

Cancer Genome Atlas Research Network (2015). The molecular taxonomy of primary prostate cancer. Cell 163, 1011–1025.

Cibulskis, K., McKenna, A., Fennell, T., Banks, E., DePristo, M., and Getz, G. (2011). ContEst: estimating cross-contamination of human samples in next-generation sequencing data. Bioinformatics 27, 2601–2602.

Cooper, C.S., Eeles, R., Wedge, D.C., Van Loo, P., Gundem, G., Alexandrov, L.B., Kremeyer, B., Butler, A., Lynch, A.G., Camacho, N., et al.; ICGC Prostate Group (2015). Analysis of the genetic phylogeny of multifocal prostate cancer identifies multiple independent clonal expansions in neoplastic and morphologically normal prostate tissue. Nat. Genet. 47, 367–372.

Cuzick, J., Swanson, G.P., Fisher, G., Brothman, A.R., Berney, D.M., Reid, J.E., Mesher, D., Speights, V.O., Stankiewicz, E., Foster, C.S., et al.; Transatlantic Prostate Group (2011). Prognostic value of an RNA expression signature derived from cell cycle proliferation genes in patients with prostate cancer: a retrospective study. Lancet Oncol. 12, 245–255.

de Bruin, E.C., McGranahan, N., Mitter, R., Salm, M., Wedge, D.C., Yates, L., Jamal-Hanjani, M., Shafi, S., Murugaesu, N., Rowan, A.J., et al. (2014). Spatial and temporal diversity in genomic instability processes defines lung cancer evolution. Science 346, 251–256.

Demichelis, F., Setlur, S.R., Beroukhim, R., Perner, S., Korbel, J.O., Lafargue, C.J., Pflueger, D., Pina, C., Hofer, M.D., Sboner, A., et al. (2009). Distinct genomic aberrations associated with ERG rearranged prostate cancer. Genes Chromosomes Cancer 48, 366–380.

Deshwar, A.G., Vembu, S., Yung, C.K., Jang, G.H., Stein, L., and Morris, Q. (2015). PhyloWGS: reconstructing subclonal composition and evolution from whole-genome sequencing of tumors. Genome Biol. 16, 35.

Ding, J., Bashashati, A., Roth, A., Oloumi, A., Tse, K., Zeng, T., Haffari, G., Hirst, M., Marra, M.A., Condon, A., et al. (2012). Feature-based classifiers for somatic mutation detection in tumour-normal paired sequencing data. Bioinformatics 28, 167–175.

Ding, Z., Mangino, M., Aviv, A., Spector, T., and Durbin, R.; UK10K Consortium (2014). Estimating telomere length from whole genome sequence data. Nucleic Acids Res. 42, e75.

Erho, N., Crisan, A., Vergara, I.A., Mitra, A.P., Ghadessi, M., Buerki, C., Bergstrahl, E.J., Kollmeyer, T., Fink, S., Haddad, Z., et al. (2013). Discovery and validation of a prostate cancer genomic classifier that predicts early metastasis following radical prostatectomy. PLoS ONE 8, e66855.

Fraser, M., Sabelnykova, V.V., Yamaguchi, T.N., Heisler, L.E., Livingstone, J., Huang, V., Shiah, Y.-J., Yousif, F., Lin, X., Masella, A.P., et al. (2017).

Genomic hallmarks of localized, non-indolent prostate cancer. Nature *541*, 359–364.

Gerlinger, M., Rowan, A.J., Horswell, S., Math, M., Larkin, J., Endesfelder, D., Gronroos, E., Martinez, P., Matthews, N., Stewart, A., et al. (2012). Intratumor heterogeneity and branched evolution revealed by multiregion sequencing. N. Engl. J. Med. *366*, 883–892.

Gonzalo, S., Jaco, I., Fraga, M.F., Chen, T., Li, E., Esteller, M., and Blasco, M.A. (2006). DNA methyltransferases control telomere length and telomere recombination in mammalian cells. Nat. Cell Biol. *8*, 416–424.

Gundem, G., Van Loo, P., Kremeyer, B., Alexandrov, L.B., Tubio, J.M.C., Papaemmanuil, E., Brewer, D.S., Kallio, H.M.L., Högnäs, G., Annala, M., et al.; ICGC Prostate Group (2015). The evolutionary history of lethal metastatic prostate cancer. Nature *520*, 353–357.

Ha, G., Roth, A., Khattra, J., Ho, J., Yap, D., Prentice, L.M., Melnyk, N., McPherson, A., Bashashati, A., Laks, E., et al. (2014). TITAN: inference of copy number architectures in clonal cell populations from tumor whole-genome sequence data. Genome Res. *24*, 1881–1893.

Halkidi, M., Gunopulos, D., Vazirgiannis, M., Kumar, N., and Domeniconi, C. (2008). A clustering framework based on subjective and objective validity criteria. ACM Trans. Knowl. Discov. Data *1*, 1–25.

Jiang, Y., Qiu, Y., Minn, A.J., and Zhang, N.R. (2016). Assessing intratumor heterogeneity and tracking longitudinal and spatial clonal evolutionary history by next-generation sequencing. Proc. Natl. Acad. Sci. USA *113*, E5528–E5537.

Klein, E.A., Cooperberg, M.R., Magi-Galluzzi, C., Simko, J.P., Falzarano, S.M., Maddala, T., Chan, J.M., Li, J., Cowan, J.E., Tsiatis, A.C., et al. (2014). A 17-gene assay to predict prostate cancer aggressiveness in the context of Gleason grade heterogeneity, tumor multifocality, and biopsy undersampling. Eur. Urol. *66*, 550–560.

Koboldt, D.C., Fulton, R.S., McLellan, M.D., Schmidt, H., Kalicki-Veizer, J., McMichael, J.F., Fulton, L.L., Dooling, D.J., Ding, L., Mardis, E.R., et al.; Cancer Genome Atlas Network (2012). Comprehensive molecular portraits of human breast tumours. Nature *490*, 61–70.

Lai, D., Ha, G., and Shah, S. (2016). HMMcopy: Copy number prediction with correction for GC and mappability bias for HTS data (R package version 0.1.1.).

Lalonde, E., Ishkanian, A.S., Sykes, J., Fraser, M., Ross-Adams, H., Erho, N., Dunning, M.J., Halim, S., Lamb, A.D., Moon, N.C., et al. (2014). Tumour genomic and microenvironmental heterogeneity for integrated prediction of 5-year biochemical recurrence of prostate cancer: a retrospective cohort study. Lancet Oncol. *15*, 1521–1532.

Lalonde, E., Alkallas, R., Chua, M.L.K., Fraser, M., Haider, S., Meng, A., Zheng, J., Yao, C.Q., Picard, V., Orain, M., et al. (2016). Translating a prognostic DNA genomic classifier into the clinic: retrospective validation in 563 localized prostate tumors. Eur. Urol. 72:22–31.

Lalonde, E., Alkallas, R., Chua, M.L.K., Fraser, M., Haider, S., Meng, A., Zheng, J., Yao, C.Q., Picard, V., Orain, M., et al. (2017). Translating a prognostic DNA genomic classifier into the clinic: retrospective validation in 563 localized prostate tumors. Eur. Urol. *72*, 22–31.

Langmead, B., Trapnell, C., Pop, M., and Salzberg, S.L. (2009). Ultrafast and memory-efficient alignment of short DNA sequences to the human genome. Genome Biol. *10*, R25.

Larson, D.E., Harris, C.C., Chen, K., Koboldt, D.C., Abbott, T.E., Dooling, D.J., Ley, T.J., Mardis, E.R., Wilson, R.K., and Ding, L. (2012). SomaticSniper: identification of somatic point mutations in whole genome sequencing data. Bioinformatics *28*, 311–317.

Li, H., and Durbin, R. (2009). Fast and accurate short read alignment with Burrows-Wheeler transform. Bioinformatics *25*, 1754–1760.

Magurran, A.E. (2004). Measuring Biological Diversity (Blackwell Pub.).

McKenna, A., Hanna, M., Banks, E., Sivachenko, A., Cibulskis, K., Kernytsky, A., Garimella, K., Altshuler, D., Gabriel, S., Daly, M., and DePristo, M.A. (2010). The Genome Analysis Toolkit: a MapReduce framework for analyzing next-generation DNA sequencing data. Genome Res. *20*, 1297–1303.

McPherson, A., Roth, A., Laks, E., Masud, T., Bashashati, A., Zhang, A.W., Ha, G., Biele, J., Yap, D., Wan, A., et al. (2016). Divergent modes of clonal spread and intraperitoneal mixing in high-grade serous ovarian cancer. Nat. Genet. *48*, 758–767.

Mermel, C.H., Schumacher, S.E., Hill, B., Meyerson, M.L., Beroukhim, R., and Getz, G. (2011). GISTIC2.0 facilitates sensitive and confident localization of the targets of focal somatic copy-number alteration in human cancers. Genome Biol. *12*, R41.

Nik-Zainal, S., Van Loo, P., Wedge, D.C., Alexandrov, L.B., Greenman, C.D., Lau, K.W., Raine, K., Jones, D., Marshall, J., Ramakrishna, M., et al.; Breast Cancer Working Group of the International Cancer Genome Consortium (2012). The life history of 21 breast cancers. Cell *149*, 994–1007.

Notta, F., Chan-Seng-Yue, M., Lemire, M., Li, Y., Wilson, G.W., Connor, A.A., Denroche, R.E., Liang, S.-B., Brown, A.M.K., Kim, J.C., et al. (2016). A renewed model of pancreatic cancer evolution based on genomic rearrangement patterns. Nature *538*, 378–382.

Pinto, D., Pagnamenta, A.T., Klei, L., Anney, R., Merico, D., Regan, R., Conroy, J., Magalhaes, T.R., Correia, C., Abrahams, B.S., et al. (2010). Functional impact of global rare copy number variation in autism spectrum disorders. Nature *466*, 368–372.

Quinlan, A.R., and Hall, I.M. (2010). BEDTools: a flexible suite of utilities for comparing genomic features. Bioinformatics *26*, 841–842.

Reimand, J., Kull, M., Peterson, H., Hansen, J., and Vilo, J. (2007). g:Profiler–a web-based toolset for functional profiling of gene lists from large-scale experiments. Nucleic Acids Res. *35*, W193–W200.

Robinson, D., Van Allen, E.M., Wu, Y.-M., Schultz, N., Lonigro, R.J., Mosquera, J.-M., Montgomery, B., Taplin, M.-E., Pritchard, C.C., Attard, G., et al. (2015). Integrative clinical genomics of advanced prostate cancer. Cell *161*, 1215–1228.

Şenbabaoğlu, Y., Michailidis, G., and Li, J.Z. (2014). Critical limitations of consensus clustering in class discovery. Sci. Rep. *4*, 6207.

Shannon, P., Markiel, A., Ozier, O., Baliga, N.S., Wang, J.T., Ramage, D., Amin, N., Schwikowski, B., and Ideker, T. (2003). Cytoscape: a software environment for integrated models of biomolecular interaction networks. Genome Res. *13*, 2498–2504.

Song, S., Nones, K., Miller, D., Harliwong, I., Kassahn, K.S., Pinese, M., Pajic, M., Gill, A.J., Johns, A.L., Anderson, M., et al. (2012). qpure: A Tool to Estimate Tumor Cellularity from Genome-Wide Single-Nucleotide Polymorphism Profiles. PLoS One *7*, e45835.

Stephens, P.J., Greenman, C.D., Fu, B., Yang, F., Bignell, G.R., Mudie, L.J., Pleasance, E.D., Lau, K.W., Beare, D., Stebbings, L.A., et al. (2011). Massive genomic rearrangement acquired in a single catastrophic event during cancer development. Cell *144*, 27–40.

Taghiyar, M.J., Rosner, J., Grewal, D., Grande, B.M., Aniba, R., Grewal, J., Boutros, P.C., Morin, R.D., Bashashati, A., and Shah, S.P. (2017). Kronos: a workflow assembler for genome analytics and informatics. Gigascience *6*, 1–10.

Taylor, B.S., Schultz, N., Hieronymus, H., Gopalan, A., Xiao, Y., Carver, B.S., Arora, V.K., Kaushik, P., Cerami, E., Reva, B., et al. (2010). Integrative genomic profiling of human prostate cancer. Cancer Cell *18*, 11–22.

Taylor, R.A., Fraser, M., Livingstone, J., Espiritu, S.M.G., Thorne, H., Huang, V., Lo, W., Shiah, Y.-J., Yamaguchi, T.N., Sliwinski, A., et al. (2017). Germline BRCA2 mutations drive prostate cancers with distinct evolutionary trajectories. Nat. Commun. *8*, 13671.

Van Loo, P., Nordgard, S.H., Lingjærde, O.C., Russnes, H.G., Rye, I.H., Sun, W., Weigman, V.J., Marynen, P., Zetterberg, A., Naume, B., et al. (2010). Allele-specific copy number analysis of tumors. Proc. Natl. Acad. Sci. USA *107*, 16910–16915.

Vogelstein, B., Fearon, E.R., Hamilton, S.R., Kern, S.E., Preisinger, A.C., Leppert, M., Nakamura, Y., White, R., Smits, A.M., and Bos, J.L. (1988). Genetic alterations during colorectal-tumor development. N. Engl. J. Med. *319*, 525–532.

Wang, K., Li, M., and Hakonarson, H. (2010). ANNOVAR: functional annotation of genetic variants from high-throughput sequencing data. Nucleic Acids Res. *38*, e164.

Weischenfeldt, J., Simon, R., Feuerbach, L., Schlangen, K., Weichenhan, D., Minner, S., Wuttig, D., Warnatz, H.-J., Stehr, H., Rausch, T., et al. (2013). Integrative genomic analyses reveal an androgen-driven somatic alteration landscape in early-onset prostate cancer. Cancer Cell *23*, 159–170.

Wilkerson, M.D., and Hayes, D.N. (2010). ConsensusClusterPlus: a class discovery tool with confidence assessments and item tracking. Bioinformatics *26*, 1572–1573.

Zhang, J., Fujimoto, J., Zhang, J., Wedge, D.C., Song, X., Zhang, J., Seth, S., Chow, C.-W., Cao, Y., Gumbs, C., et al. (2014). Intratumor heterogeneity in localized lung adenocarcinomas delineated by multiregion sequencing. Science *346*, 256–259.

STAR★METHODS

KEY RESOURCES TABLE

REAGENT or RESOURCE	SOURCE	IDENTIFIER
Deposited Data		
Cytoband file for hg19 (v2016-09-21)	University of California, Santa Cruz	http://hgdownload.cse.ucsc.edu/downloads.html
Cosmic Signatures	Wellcome Trust Sanger Institute	http://cancer.sanger.ac.uk/cosmic/signatures
WGS Data – Baca	Baca et al., 2013	dbGaP Study Accession: phs000447.v1.p1
WGS Data – Berger	Berger et al., 2011	dbGaP Study Accession: phs000330.v1.p1
WGS Data – CPC-GENE	Fraser et al., 2017	EGA Study ID: EGAS00001000900; GEO: GSE84043
WGS Data – TCGA	The Cancer Genome Atlas Research Network, 2015	https://portal.gdc.cancer.gov/projects/TCGA-PRAD
WGS Data - Weischenfeldt	Weischenfeldt et al., 2013	EGAS00001000400
WGS Data – CPC-GENE	This study	EGAS00001000900
Experimental Models: Cell Lines		
Transplantable metastasis model	Jiang et al., 2016	http://www.pnas.org/content/113/37/E5528.long?tab=ds
Software and Algorithms		
BEDTools (v2.17.0)	Quinlan and Hall, 2010	https://github.com/arq5x/bedtools2
GISTIC2.0 (v2.0.22)	Mermel et al., 2011	http://portals.broadinstitute.org/cgi-bin/cancer/publications/view/216
Qpure (v1.1)	Song et al., 2012	https://sourceforge.net/projects/qpure/
ASCAT (v2.1)	Van Loo et al., 2010	https://github.com/Crick-CancerGenomics/ascat
bwa-aln (v0.5.7)	Li and Durbin, 2009	http://maq.sourceforge.net
GATK (v2.4.9)	McKenna et al., 2010	https://software.broadinstitute.org/gatk/
ContEst (v1.0.24530)	Cibulskis et al., 2011	http://www.broadinstitute.org/cancer/cga/contest
SomaticSniper (v1.0.2)	Larson et al., 2012	http://gmt.genome.wustl.edu/packages/somatic-sniper/
TelSeq (v0.0.1)	Ding et al., 2014	https://github.com/zd1/telseq
TITAN (v1.11.0)	Ha et al., 2014	https://github.com/gavinha/TitanCNA
HMMcopy (v0.1.1)	Lai et al., 2016	http://bioconductor.org/packages/release/bioc/html/HMMcopy.html
Bowtie (v2.2.6)	Langmead et al., 2009	https://github.com/BenLangmead/bowtie
Kronos (v1.12.0)	Taghiyar et al., 2017	https://pypi.python.org/pypi/kronos-pipeliner
MutationSeq (v4.3.7)	Ding et al., 2012	http://shahlab.ca/projects/mutationseq/
PhyloWGS (v2016-06-21)	Deshwar et al., 2015	https://github.com/morrislab/phylowgs
ANNOVAR (v2015-06-17)	Wang et al., 2010	http://annovar.openbioinformatics.org/en/latest/user-guide/download/
ConsensusClusterPlus (v1.24.0)	Wilkerson and Hayes, 2010	https://bioconductor.org/packages/release/bioc/html/ConsensusClusterPlus.html
gprofileR (v0.6.1)	Reimand et al., 2007	https://biit.cs.ut.ee/gprofiler/
Cytoscape (v3.4.0)	Shannon et al., 2003	http://www.cytoscape.org/

CONTACT FOR REAGENT AND RESOURCE SHARING

Further information and requests for resources should be directed to and will be fulfilled by the Lead Contact, Paul C. Boutros (Paul. Boutros@oicr.on.ca).

EXPERIMENTAL MODEL AND SUBJECT DETAILS

Patient Cohort

We analyzed the genomic data accrued from a cohort of 293 retrospective localized prostate tumors with patient consent and Research Ethics Board approval using published whole-genome sequences of tumor samples drawn from the index lesion of the tumor and matched blood-based normal reference samples (Baca et al., 2013; Berger et al., 2011; Cancer Genome Atlas Research Network, 2015; Fraser et al., 2017; Weischenfeldt et al., 2013). All patients were male and ranged in age from 38-81 years at diagnosis. For surgery patients, the index tumor was identified macroscopically by a GU expert pathologist at the point of surgery, and subsequently sampled and biobanked. A fresh-frozen tissue specimen from this index lesion was then obtained for macro-dissection. For radiotherapy patients, the index tumor was identified on transrectal ultrasound and sampled by needle biopsies (TRUS-Bx) and was deemed to be the largest focus of disease that was pathologically confirmed. A fresh-frozen needle core ultra-sound-guided biopsy to this index lesion was obtained for macro-dissection. All frozen specimens were retrieved, sectioned, and reviewed by the GU pathologist for tumor cellularity and Gleason Score. These were compared against the histomorphology of the primary surgical specimen for patients who underwent surgery. Patients were offered standard-of-care treatment, with no randomization or rule-based classification to radiotherapy or surgery. All specimens were reviewed for Gleason grade and cellularity, and we focused on patients with clinical intermediate-risk disease by NCCN criteria. Briefly, this involves patients with T2b or T2c disease or having tumors with a Gleason Grade of 7 or having pre-treatment serum PSA of 10-20 ng/mL. Follow-up is ongoing, with a median follow-up of 8.85-years. Up to 200 ng of DNA from these fresh-frozen samples were hybridized to Affymetrix OncoScan arrays for SNP and CNA profiling. Whole-genome sequencing from 50 ng of DNA or more from fresh-frozen tumor was completed on Illumina HiSeq 2000 or HiSeq X Ten sequencers. WGS and microarray protocols for data generation have been described previously (Fraser et al., 2017). Assays were not blinded.

Transplantable Metastasis Model

The transplantable metastasis model system has been previously described in detail (Jiang et al., 2016). In brief, the parental human female breast cancer cell line MDA-MB-231 was obtained from the American Type Tissue Collection and engrafted into mouse models to induce organ-specific metastasis. The phenotypically stable and metastatically competent derivative cell lines were grown from *in vivo* selected single-cell or mixed-cell populations from bone and lung metastasis. Exome sequencing was performed on the parental and derived cell lines.

METHOD DETAILS

SNP Microarray Data Analysis

We identified CNV and SNP profiles using Affymetrix OncoScan FFPE Express 2.0 and 3.0 assays. To summarize, copy number segments were identified and annotated with RefGene (2014-07-15) and BEDTools (v2.17.0) (Quinlan and Hall, 2010). Recurrent calls were filtered using a 75% threshold in the normal samples. CNA segments were generated using GISTIC2.0 (v2.0.22) (Mermel et al., 2011) and the average intensity of each segment was obtained from SNP arrays. qpure (v1.1) (Song et al., 2012) and ASCAT (v2.1) (Van Loo et al., 2010) algorithms estimated cancer cellular purities using data from the SNP arrays. Full details are given elsewhere (Fraser et al., 2017).

Whole-Genome Sequencing Data Analysis

For each tumor, bwa-aln (v0.5.7) (Li and Durbin, 2009) was used to align the tumor and normal FASTQ files against build hg19 of the human genome. These BAMs were then locally realigned and subject to quality-score recalibration using GATK (v2.4.9) (McKenna et al., 2010), followed by lane- and sample-level sample mixup checking and lane-level cross-individual contamination assessment using ContEst (v1.0.24530) (Cibulskis et al., 2011). SomaticSniper (v1.0.2) (Larson et al., 2012) was then run on the aligned, recalibrated BAMs to generate predicted somatic SNVs. Full details are given elsewhere (Fraser et al., 2017). Telomere length was estimated, ignoring read groups, using TelSeq (v0.0.1) with default parameters (Ding et al., 2014).

Somatic Subclonal Copy Number Assessment

Subclonal CNAs were identified from the whole-genome sequencing data using TITAN (v1.11.0) (Ha et al., 2014). First, GC and mappability files were prepared from the reference file using the BioConductor package HMMcopy (v.0.1.1) (Lai et al., 2016) and bowtie (v2.2.6) (Langmead et al., 2009). We referred to the practices outlined here: http://bioconductor.org/packages/release/bioc/html/HMMcopy.html. Next, the Kronos (v1.12.0) pipeline (Taghiyar et al., 2017) was used to preprocess the whole-genome data and run TITAN (v1.11.0) to generate the copy number calls. MutationSeq (v4.3.7) (Ding et al., 2012) determined the heterozygous positions in the data using the known dbSNP sites from GATK (v2.4.9) (McKenna et al., 2010). The GC and mappability files accounted for any biases in the data, prior to running TITAN (v1.11.0). TITAN (v1.11.0) (Ha et al., 2014) was run across an input range of one to five clusters, representing the exact number of subclones to be predicted. The set of parameters to be used was determined by optimizing for the lowest S_Dbw validity index (Halkidi et al., 2008), and the resulting CNAs were used in all further analysis. For benchmarking, MuTect (v1.1.4) was used with the default parameters except -tumor_lod option (tumor limit of detection), which was

set to 10. We then retained only the confident SNVs by filtering out any calls marked by REJECT. Battenberg (v2.2.6) was used via the cgpBattenberg installation wrapper (v3.1.0) with default parameters and supplemental files generated using developer instructions.

Phylogenetic Reconstruction of Tumors

To reconstruct the evolution of the tumor, we used the cnv-int branch of PhyloWGS (Deshwar et al., 2015) (https://github.com/morrislab/phylowgs/tree/cnvint, commit: 3b75ba9c40cfb27ef38013b08f9e089fa4efa0c0), in order to take into account both SNVs and CNAs. We used the parse_cnvs.py script to parse the TITAN (v1.11.0) optimal predicted CNA segments and tumor cellularities, and filtered any entries that were 1-bp TITAN CNAs. Further, these filtered CNAs and the high confidence SomaticSniper (v1.0.2) variant calls made on callable bases were inputted into the create_phylowgs_inputs.py script to generate PhyloWGS inputs. As a final CNA filter, we also removed any CNA entries generated that had a total read depth of 0. In addition, we annotated each SNV with the gene (if any) associated with the mutation as given by ANNOVAR (v2015-06-17) (Wang et al., 2010). Using default parameters, PhyloWGS evolve.py script generated possible tree structures for each tumor. The JSON results were parsed to determine the best consensus tree, given by the largest log likelihood value, and the SNVs and CNAs associated with each subclone in the best predicted structure (Figure S1A).

Phylogenetic trees were then aggregated across the cohort. The node numberings and edge connections in PhyloWGS trees were hierarchized by subclone cellular prevalence and thus not translatable across different samples with the same overall evolutionary trajectory. With the root node (normal population) labeled as 0, each consensus tree was transformed according to two rules (Figure S1B):

1. Nodes at depth *i* are labeled a lower number than all nodes at depth *j*, where *j* > *i.*
2. Trees are left-heavy.

Notice that in the example the two tree structures were the same. For each individual tumor tree, we ensured that each node had at least 5 SNVs or 5 CNAs. Nodes that did not satisfy the criteria were: 1) merged with its parent node, if it has no siblings (its parent has no other child); 2) merged with its siblings; or 3) eliminated if it is the only direct child of the normal node. The eliminated node's children become the direct descendants of the normal (Figure S1C). This conservative approach was very rare across the cohort, changing tree structure for 13/293 tumors, including 7 for which a clone was supported by either a single CNA or a single SNV and a single CNA. This heuristic leads our pipeline to be conservative and to be a lower bound on the true subclonal diversity of a tumor. When PhyloWGS returned a polytumor solution, it was re-run with a different random number generator seed up to twelve times, after which a polytumor solution was accepted. This procedure was designed to provide a lower bound on the frequency of polytumors. The order of seeds used was: 12345, 123456, 1234567, 12345678, 123456789, 246810, 493620, 987240, 1974480, 3948960, 7897920, and 15795840.

Cell Line Validation

To validate our approach, we applied phylogenetic inference using PhyloWGS to a transplantable metastasis model where ground truth is known (Jiang et al., 2016). CNA detection used SynthEx (v1.5) and freebayes (v1.0.0) parameterized as recommended by the developers. SNV detected using MuTect (v1.1.7) with panel of normal derived from TCGA Breast Invasive Carcinoma samples (Koboldt et al., 2012). We recovered the subclonal composition of the bone metastasis mixed cell population (MCP)-derived cell line. Further, we showed that the lung metastasis MCP-derived cell lines have similar composition despite possible artifacts in subclone identification (Figures S1H–S1K).

QUANTIFICATION AND STATISTICAL ANALYSIS

Scoring Tree Structures

To quantify the subclonal diversity of each tumor sample by the number and abundance of subclones, we calculated the Shannon diversity index (H) (Magurran, 2004) by the equation:

$$H = -\sum_i p_i \ln(p_i)$$

where p_i is the abundance of clone *i* in tumor. Clonal abundance is calculated using the CCF (cancer cell fraction) of each node, subtracted by the total CCF of its children, as to give the percentage of cells still belonging to the subclone in the tumor.

Classifying Mutations

Using the consensus trees generated by PhyloWGS, we classified mutations (both CNAs and SNVs) as occurring in the trunk or branch of the tree. Trunk mutations encompassed those that occurred between the root node (normal) and its only child node, while all others were classified to have occurred in branch.

Representative Tree Structures

We aggregated the patients based on their tumour tree structures. For each patient, the rank product was calculated by multiplying the rank in terms of the number of SNVs, CNAs measured by total PGA, and tumor purity. Each condensed tree was represented by the median tree. For each node of the tree, we calculated one standard deviation from the median tree cellularity across the entire population of nodes at this position in all identical trees.

Subclonal Analysis of Recurrent Mutations

We identified recurrent coding SNV mutations and classified them as have occurred in trunk or branch. All SNVs assigned by PhyloWGS were filtered against blacklists of known sequencing artifacts and germline contaminants, and whitelists of recurrent COSMIC (v70) mutations. Nonsynonymous, stop-loss, stop-gain or splice-site SNVs were considered as functional (based on RefGene annotations). For each gene that was recurrently mutated at 2% or higher (with functional SNVs in more than 6 patients), or previously identified as recurrently mutated (Fraser et al., 2017), we calculated the proportion of SNVs that have occurred in trunk. We used Fisher's exact test to check for significance of whether the gene was preferentially mutated in the trunk or in the branch.

For non-coding SNVs (ncSNVs) assigned by PhyloWGS, we considered only those that have been previously identified as recurrent (Fraser et al., 2017). We calculated the proportion of each recurrent ncSNVs that have occurred in trunk and used Fisher's exact test to check for significance.

CNAs identified by PhyloWGS were assigned to have occurred in the trunk or branch. The CNAs for patients that had OncoScan data were further filtered against those reported by the technology, retaining only the TITAN-predicted CNA that had overlapped. For patients lacking OncoScan data, we used the mean recurrence across the other patients in each chromosome. We considered bins of 1 Mbp across the genome and set the CNA indicator to one for all patients that had a CNA overlapping with that 1 Mbp stretch. We then compared the presence of truncal and branch CNAs across the patients and identified 13 groups of significantly different CNAs (Pearson's χ^2 test; multiple correction using FDR; $q \leq 0.10$). Groups were determined by their cytoband location. Bins that were within 20 Mbp of each other were considered as the same group.

Consensus clustering was applied separately to the trunk and branch CNA profiles using the ConsensusClusterPlus package (v1.24.0), customized to include the Jaccard distance metric (trunk: distance = Euclidean, pItem = 0.8, finalLinkage = Ward.D2, innerLinkage = Ward.D2; branch: distance = Jaccard, pItem = 0.8, finalLinkage = Ward.D2, innerLinkage = Ward.D2) (Wilkerson and Hayes, 2010). The optimal cluster number was selected by minimizing the proportion of ambiguous clustering value (Şenbabaoğlu et al., 2014). Loci were determined by position from a cytoband file for hg19 downloaded on 2016-09-21 from http://hgdownload.cse.ucsc.edu/downloads.html, or by invoking the command: curl –s http://hgdownload.cse.ucsc.edu/goldenPath/hg19/database/cytoBand.txt.gz | gunzip -c > cytoBand.txt

Pathway Analysis

The genes involved in the 13 groups of significantly different CNAs were analyzed further for pathway enrichment. Using gprofileR (v0.6.1) in R (v3.2.5) (Reimand et al., 2007), all statistically significant pathways were obtained from default parameters and the data sources Gene Ontology (Biological Process, Molecular Function, and Cellular Component), KEGG and Reactome. Pathways that involved more than 700 or fewer than 5 genes were discarded (Pinto et al., 2010).

To identify pathways that were significantly differentially affected in the trunk and branch, we used Fisher's exact test to assess whether the gene-set was more frequently affected by trunk or branch CNAs and label permutations to determine their significance (Pinto et al., 2010). For each patient, the trunk and branch CNA profiles were separately used to determine the gene-sets affected. A pathway was considered to be affected if the CNAs implicated at least one gene belonging to the gene-set. As the CNAs belonged to either trunk or branch, the location status of the set of pathways affected were respectively classified as trunk or branch. After initial assignment, we permuted the location status of pathway sets 1000 times so that the CNA events were independent of location assignment. The p values generated from Fisher's Exact Test through the iterations were used to build the null hypothesis distribution and pathways with q < 0.05 were considered significant. Significant pathways were visualized using Cytoscape (v3.4.0) (Shannon et al., 2003).

Subclonal Analysis of Kataegis

To quantify where and when kataegis events occurred, we used the sliding window binomial test approach as described previously (Fraser et al., 2017). Each subclone of every patient was considered separately, with all of its post-filter SNVs assigned by PhyloWGS in the consensus tree, as to pinpoint where the kataegis events occurred in tumor evolution. A rainfall plot with the x axis as SNV position and the y axis as the log transformed inter-mutational distance was generated to represent all of the SNVs in all of the patients that had at least one kataegis event, with the SNVs involved in the events highlighted using their timing of occurrence.

Trinucleotide Mutation Signatures

We used TrackSig to estimate signature exposures across the evolutionary history of each individual tumor (https://doi.org/10.1101/260471). We used cancer cell fraction (CCF) as an estimate of relative of mutation occurrence. We assumed that mutations with higher CCF occurred earlier than the ones with lower CCF. Thus, CCF can be viewed as pseudo-time of mutation occurrence.

To construct the timeline, we sorted mutations based on decreasing CCF and divided them into bins of four hundred. Each bin corresponds to one time point, and in each subsequent time point the bin was moved by one hundred mutations in a sliding window manner. Within a time point we separated mutations into 96 categories based on trinucleotide context and fit the mutational signatures to those counts using mixture of multinomials. We use a set of 30 signatures from COSMIC (http://cancer.sanger.ac.uk/cosmic/signatures). Signatures are represented as multinomial distributions over 96 types of mutations. Though mixture of multinomial modeling, we obtain mixture coefficients, which correspond to exposures of the mutational signatures in each bin.

Time points when signature profiles change substantially represent loss or gain of different mutational processes. We used a greedy search algorithm to find the change points in signatures trajectories and used Bayesian Information Criterion to estimate the optimal number of change points. Thus, signature exposures are represented as trajectories across the CCF timeline.

We evaluated uncertainty by bootstrapping sets of mutations and re-computing exposure estimates 30 times. The standard deviation of the exposures at each time point was used as an uncertainty estimate over exposures and plotted as shaded area around the trajectory.

Not all of the signatures are active in the tumor at the same time. The signatures active in the sample depend on the cancer type and environment. To determine active signatures in a sample, we fit all 30 COSMIC signatures and chose a subset of signatures that have exposure > 5%. We refit the signature trajectories as described above using the selected set of signatures.

We plotted the computed exposures as trajectories on the decreasing CCF scale. Each mutation bin is assigned a CCF value based on the average CCFs of the SNVs in the bin. We plot the trajectories averaged across 30 bootstrap runs. Signatures that were not in the subset of six signatures most active in our samples (i.e., S1, S3, S5, S8, S9 and S16) or did not reach 20% at any time point were excluded from visualizations. See doi: https://doi.org/10.1101/260471.

Subclonal Tree Correlations

We used Spearman's ρ to test for associations with age at diagnosis, PSA, clinical Gleason Score, T-category and ERG fusion status. We compared these to a set of tree features comprising PhyloWGS subclone counts, tree depth, proportion of SNVs in trunk, proportion of CNAs, in trunk, Shannon Index, total PGA, PGA accumulated in trunk and kataegis events. Additional associations were tested among these tree correlates as well as tumor cellularity. Only *polyclonal* samples were analyzed as they have both a trunk and a branch. CNAs Trunk and SNVs Trunk refer to the proportion of CNAs and SNVs in the trunk, respectively. PGA Overall refers to the total PGA in the sample while PGA Trunk refers to PGA in the trunk node only.

Microarray Sensitivity

We split the filtered TITAN CNAs into trunk and branch ones, creating separate gene by patient matrices. For each patient we then considered what proportion of genes with TITAN CNAs was identified to have CNAs using OncoScan microarrays. We tested for differences between the proportion of trunk CNAs detected and the proportion of branch CNAs detected with a Mann-Whitney U-test.

Survival Analysis

The tumors were arranged into two distinct clonality groups: *monoclonal* tumors only derive one clonal population in its evolution, while *polyclonal* includes the remainder, with at least one subclonal population. We assessed differences in outcome by fitting a Cox proportional hazard regression model, reporting the p value from the Wald test. Multivariate analyses were carried out to correct for known prognostic clinical variables (clinical Gleason Score, clinical T-category and pre-treatment PSA), and the power to detect subclones (reads per cancer cell, number of SNVs and number of CNAs). The proportional hazards assumption was verified by examination of the Schoenfeld residuals and, for multivariate analyses, global Pearson's χ^2 tests. Primary outcome was time to BCR, defined to be a PSA rise of $\geq$ 2.0 ng/mL above the nadir PSA for patients who underwent image-guided radiotherapy. For patients who underwent surgery, BCR was defined as two consecutive post-surgery PSA measurements > 0.2 ng/mL (backdated to the date of the first increase), as long as the patient had a post-surgery PSA < 0.2 ng/mL, otherwise this was considered a primary treatment failure rather than a BCR event. If a patient had successful salvage radiation therapy, the patient was not considered to have a BCR. If PSA continued to rise after salvage radiation therapy, BCR was backdated to the first PSA measurement > 0.2 ng/mL. If a patient received other salvage treatment (such as hormonal therapy or chemotherapy), this is considered a BCR.

Scoring Biomarker Signatures

The proportion of the genome altered (PGA) was calculated for each cancer cell population in a patient's tumor, where every population harbors all of the CNAs that have occurred in its evolutionary history. Trunk PGA was calculated from trunk CNAs, while branch PGA was calculated from the CNAs that have occurred between the clonal node and the most altered subclonal node. PGA was calculated by summing the total number of bases covered by the CNAs and divided by the total size of the whole genome. We used the previously validated at-risk threshold of PGA $\geq$ 7.49%: patients below this value are predicted to have good prognosis, and patients equal to or above it are predicted to have poor prognosis (Lalonde et al., 2017).

To confirm the PGA results, we also used a validated prognostic 100-locus CNA signature for localized prostate cancer to assess the risk of each patient (Lalonde et al., 2014). This signature was applied to each clonal population in a patient's tumor in the same

way as for PGA: the patient risk score resulting from only the clonal node is the trunk risk score, while the gain in risk score between the clonal and the subclone with the highest risk is defined as the branch risk score. We retained the published and validated at-risk threshold for this signature of 0.5, with scores lower than this indicating good prognosis and those equal to or higher predicting poor prognosis. We used Cox proportional hazard models and area under the receiver operator curve to assess differences in biomarkers applied to different nodes. Scores from the multi-modal biomarker signature are shown in Table S1. Reporting of analysis of prognostic signatures follows the REMARK recommendations.

Data Visualization and Reporting

Plotting was performed in the R statistical environment (v3.2.5) using the lattice (v0.20-34), latticeExtra (v0.6-28) and BPG (v5.3.4; doi: https://doi.org/10.1101/156067) packages. Figures were also compiled using Inkscape (v0.48) and Cytoscape (v3.4.0). Point estimates for the mean were reported along with a 95% confidence interval for the population mean. Unless otherwise stated, all statistical tests are two-sided. In Figure 1B, the representative tree for each tree structure was selected by calculating the rank product of the number of SNVs, PGA, and tumor purity. The tree with the median rank-product was selected for visualization. All trees are shown in Data S1. Grade Groups reported in all figures correspond to the specific tumor specimen used for genomic analyses.

DATA AND SOFTWARE AVAILABILITY

The accession number for the raw sequencing data reported in this paper is European Genome-phenome Archive: EGAS00001000900 (https://www.ebi.ac.uk/ega/studies/EGAS00001000900). Processed variant calls are available through the ICGC Data Portal under the project PRAD-CA (https://dcc.icgc.org/projects/PRAD-CA). A high-resolution version of Data S1 is available at https://labs.oicr.on.ca/boutros-lab/projects/200pt.
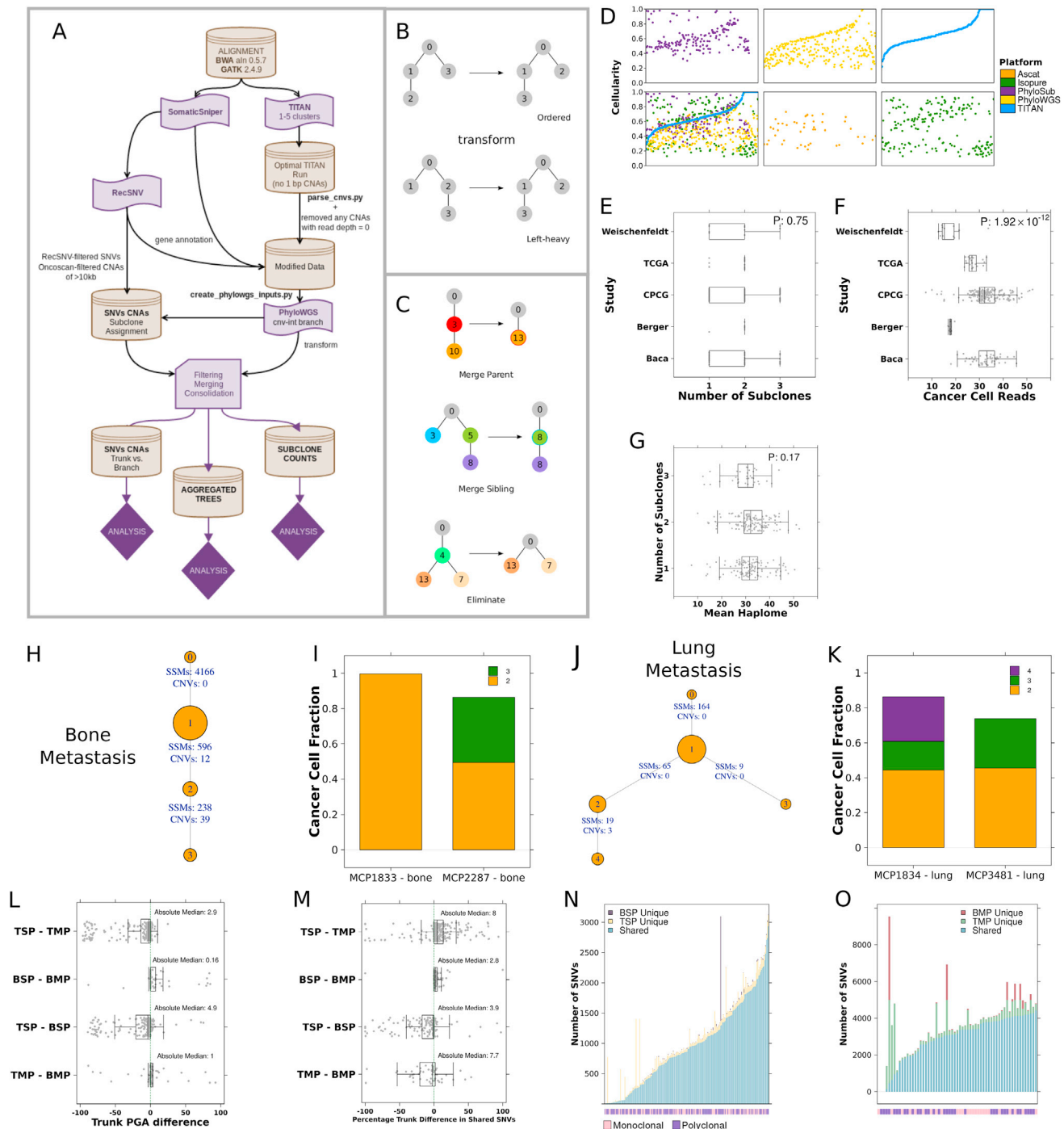
Figure S1. Reconstruction Workflow, Related to Figure 1

(A) Analysis workflow, starting from raw sequencing data and ending with processed and annotated trees.

(B) Intermediate processing step in which PhyloWGS-reconstructed trees were aggregated across the cohort. Nodes are initially numbered according to PhyloWGS nomenclature, then transformed to a hierarchical structure.

(C) Intermediate processing step that determines if a node has sufficient mutations, or will be merged. Nodes are labeled by the number of mutations they have and color-coded based on the subclone they arise from. This represents cases when a node is merged with its parent, merged with its sibling and when it is eliminated.

(D) Cellularity estimates from PhyloWGS, PhyloSub, TITAN, ASCAT and ISOpure. The bottom left shows an overlay of all methods while the other panels show different estimation methods. Each dot shows the estimate for a sample. Samples are ordered by TITAN cellularity estimates.

(E) shows the number of subclones detected as a function of the study in which the data were generated.

(F) shows the sample coverage corrected by ploidy, to give reads per cancer chromosome, as a function of the study in which the data were generated.

(G) shows the distribution of per-tumor coverage by the number of subclones detected. p values from a Kruskal-Wallis test are shown in plots (E–G).

(H–K) Tree structures and sample subclonal composition of cell-line transplantable metastasis models from Jiang et al. Trees show relationships between subclones with subclone one representing the clonal population and all others representing subclonal populations. Barplots show the subclonal composition of each cell line sample. (H and I) The results from a bone metastasis mixed cell population (MCP)-derived cell line. (J and K) Results from a lung metastasis MCP-derived cell line are shown. These results recapitulate the known phylogeny of these cell line populations.

(L–O) We also compared tree characteristics across four phylogenetic reconstruction methods: TSP: TITAN + SomaticSniper + PhyloWGS; TMP: TITAN + MuTect + PhyloWGS; BSP: Battenberg + SomaticSniper + PhyloWGS; BMP: Battenberg + MuTect + PhyloWGS. (L) Differences in clonal PGA between comparable methods. Absolute median is the median of the absolute values of differences. Differences in percentage of clonal SNVs between methods considering only SNVs found in both resulting trees are shown in (M). Shared and unique SNVs in phylogenetic trees from different methods that use the same SNV caller are shown in (N) and (O). SNV presence in the tree depends on the subclonal CNA calls of the region. The covariates on the bottom indicate tree structure based on TSP.
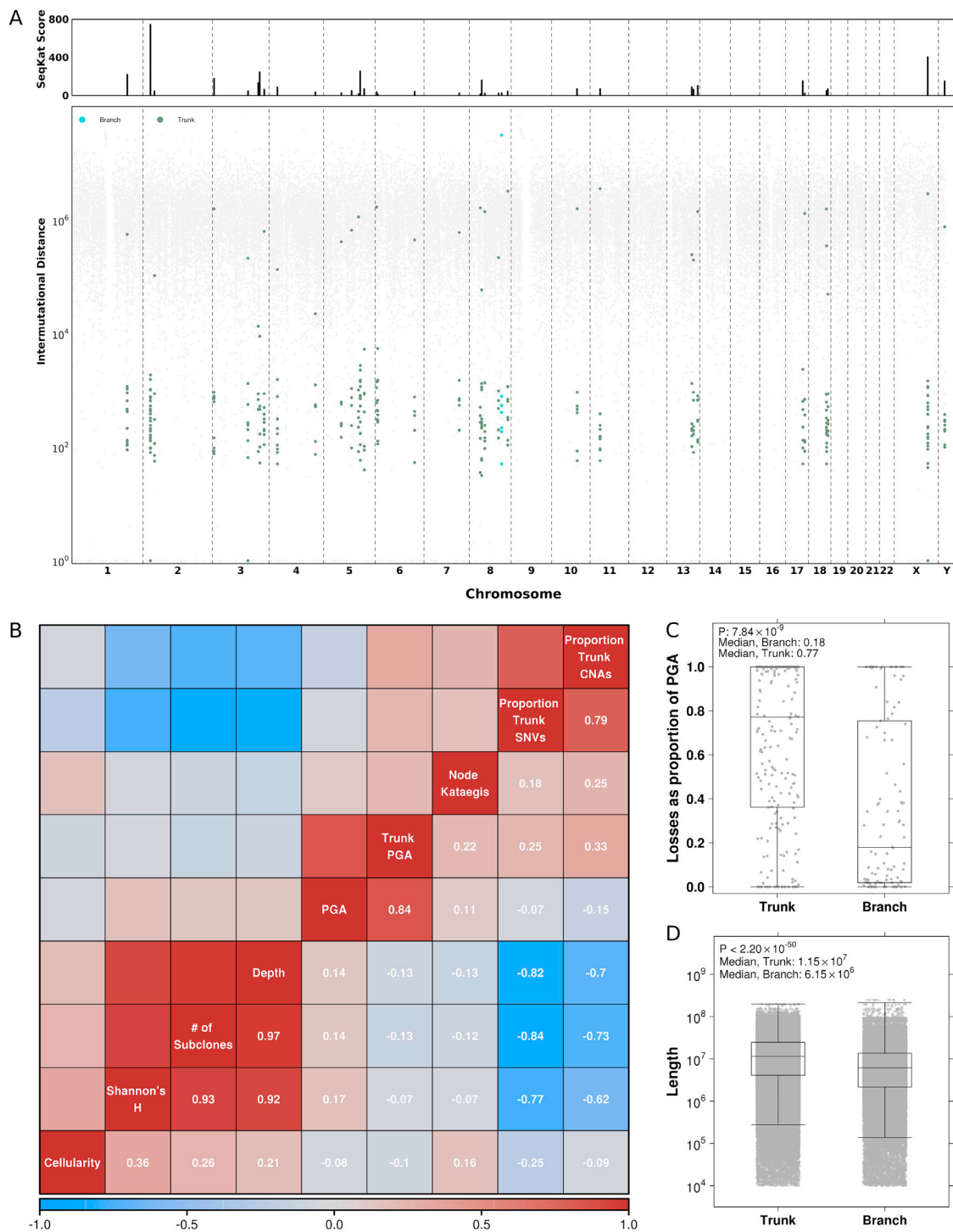
Figure S2. Mutational and Evolutionary Hallmarks of Subclonality, Related to Figure 2

(A) Kataegic events across all samples, with each dot representing an SNV and the coloring specifying whether an SNV is part of a kataegic event in trunk or branch. Within a kataegic cluster of mutations, inter-mutational distances are calculated. Kataegis score measures the significance of deviation, from expected, within these clusters.

(B) Correlations between tree characteristics (Table S1; STAR Methods) using Spearman's ρ.

(C) shows the proportion of 1 Mbp bins that contain a CNA that are predominantly losses: an estimate of loss-only PGA, with p value from a Mann-Whitney U-test.

(D) compares CNA lengths in the trunk and branch, with p value from a Mann-Whitney U-test.
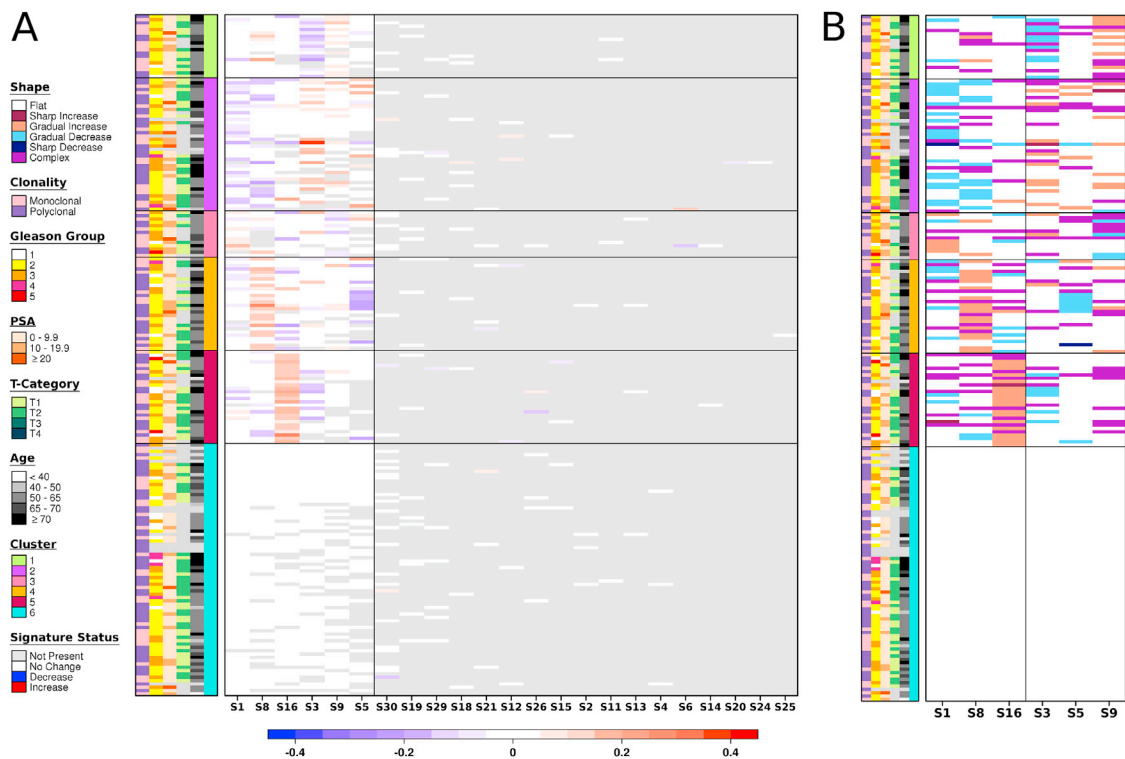
Figure S3. Trinucleotide Mutation Signature Distributions, Related to Figure 3

(A) Change of exposure level per signature, across all time points in samples with more than 600 SNVs.

(B) Shape of each signature by sample, as characterized by change-points with non-overlapping error bars. Patients were clustered using consensus clustering and sorted by signature change within each cluster.
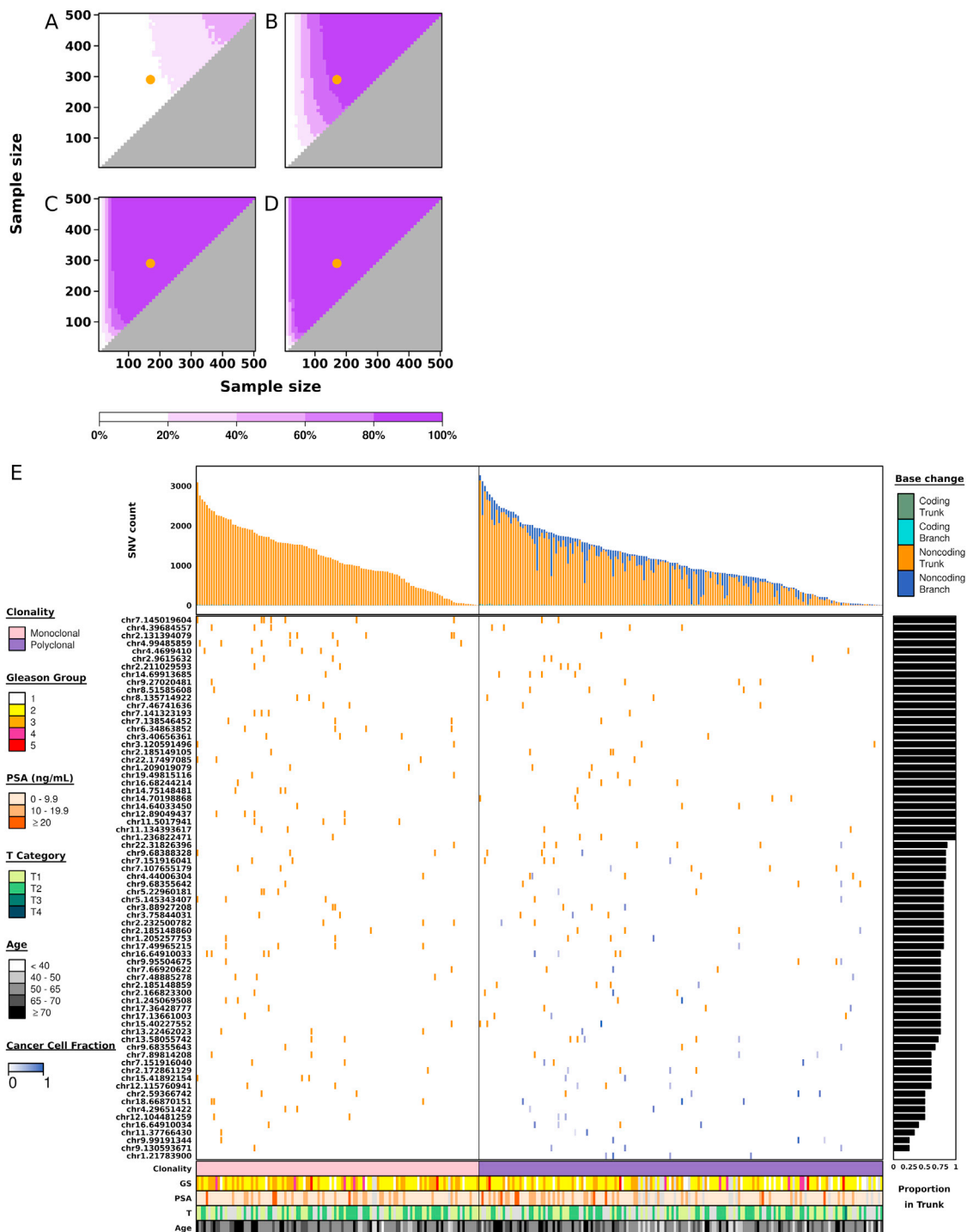
Figure S4. Differential Trunk-Branch SNV Mutation Frequency, Related to Figure 4

(A–D) Power analysis for tests of whether coding SNVs occur preferentially in trunk or branch, based on Fisher's exact test and Bonferroni correction for 20 tests. Effect sizes 0.2, 0.4, 0.6, and 0.8, respectively. The orange dots indicate the sample size of this study (n = 289 total, of which n = 146 are polyclonal). The background color indicates the statistical power.

(E) Non-coding SNVs previously identified as recurrent were classified as trunk or branch. Samples are ordered by tree-type and the total number of SNVs (both coding and non-coding). Non-coding SNVs are sorted by their proportion of occurrence in the trunk and frequency.
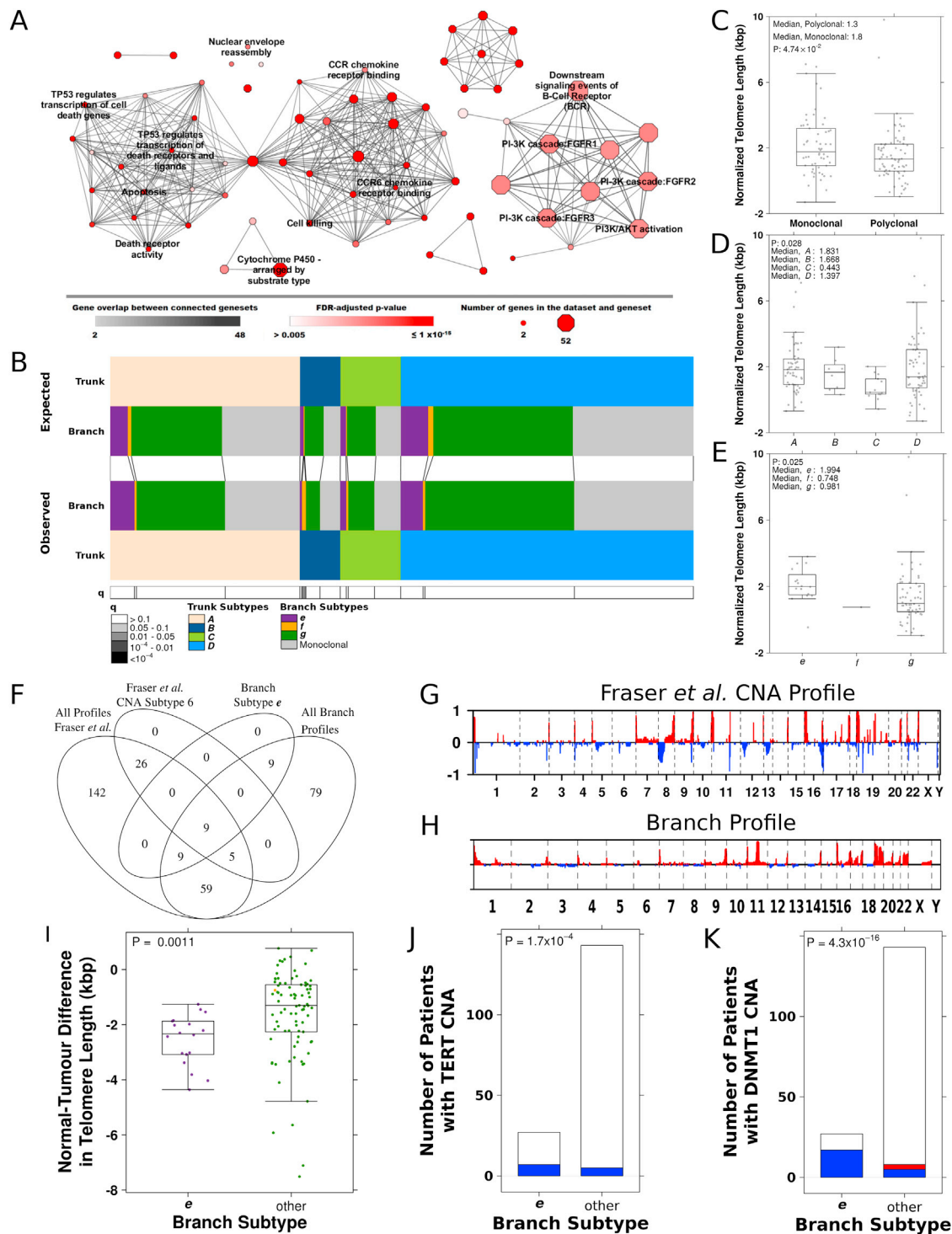
Figure S5. Pathway and Subtype Hallmarks of Subclonal CNAs, Related to Figure 5

(A) Enrichment map showing pathways (Q < 0.05, multiple testing correction using FDR) related to CNAs that were enriched in the trunk or branch from using Gene Ontology, KEGG, and Reactome. Enriched pathways from g:Profiler (Reimand et al., 2007) were filtered via permutation analysis and filtered pathways visualized with Cytoscape (v3.4.0).

(B) The concordance of trunk and branch subtypes is shown by comparing the expected proportion (top) to the observed proportion (middle) of patients in the pair subtypes along the x axis. At the bottom is the Q-value assessing whether the proportion of patients classified in each pair of subtypes differs from that expected by chance alone (Fisher's Exact test).

(legend continued on next page)

(C) compares normalized telomere length differences (estimated with TelSeq [Ding et al., 2014]) between monoclonal and polyclonal tumors (Mann-Whitney U-test).

(D and E) Telomere lengths of patients clustered into trunk and branch CNA subtypes, respectively, with the corresponding Kruskal-Wallis test p value.

(F) Patient-wise overlap between subtypes having sub-telomeric gains.

(G and H) The average profile for the 27 patients in branch subtype *e* are shown in (G) using the CNA profiles from Fraser et al. (2017) and in (H) using the derived branch profiles. Gene gains are represented in red and gene losses in blue.

(I) The difference between estimations of telomere length in the normal and tumor (Fraser et al. 2017) samples is shown with the corresponding two-sided Wilcoxon test p value comparing *e* patients to all others.

(J and K) Subtype *e* is enriched for patients with (J) gain of *TERT* and (K) loss of *DNMT1* in the overall (Fraser et al. 2017) CNA profiles, testing for equal proportions using Pearson's χ^2 test.
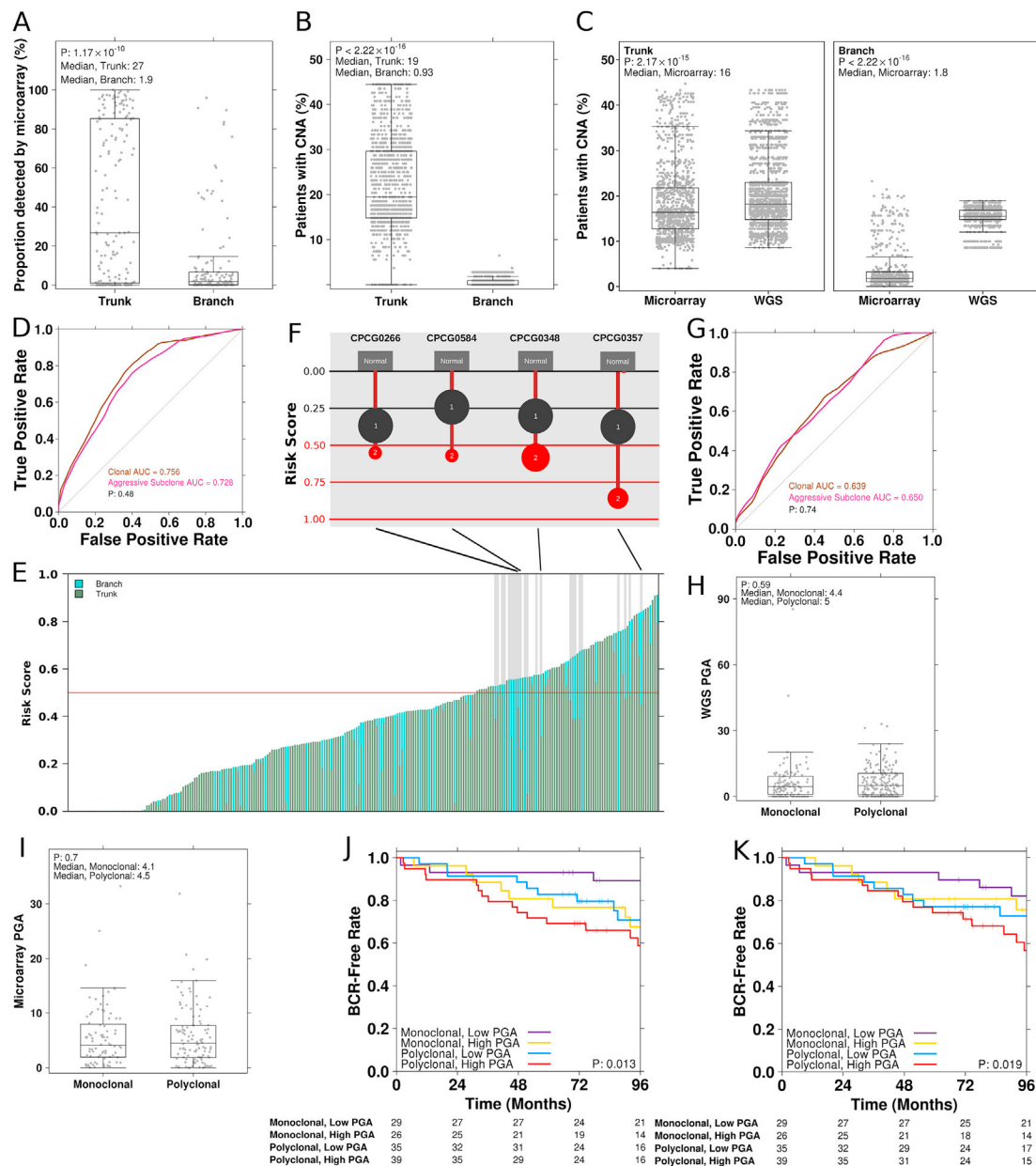
Figure S6. Differential Risk Classification across Technologies, Related to Figure 6

(A) Proportion of WGS-detected CNAs in the trunk and branch that were detected by microarrays in matched DNA aliquots.

(B) Recurrence of CNAs in the genes identified as differentially altered in trunk and branch are shown for microarray data from an independent patient cohort (Taylor et al., 2010).

(C) Gene-level recurrence across technologies in the cohort from the current study, demonstrating much higher agreement for trunk than branch aberrations. p values from Mann-Whitney U-tests are shown in (A)–(C).

(D) shows that the area under the receiver operator curve (AUC) is unchanged for the 100-locus risk score signature applied to the trunk and to the subclone with the highest risk score.

(E and F) Risk score of 100-locus biomarker calculated for trunk mutations only, and all mutations in the tumor. The red line divides the low-risk (risk score < 0.5) from the high-risk (risk score ≥ 0.5) patients. Bars with a gray background indicate patients that are pushed to being high risk when considering CNAs that occur in their subclonal populations. Exemplars of these cases are shown in (F). Red outlines the turning point in which the patient becomes high risk.

(G) Shows the area under the receiver operator curve (AUC) is unchanged for PGA calculated with either a cutoff of 7.49% applied to trunk alone or the subclone with the highest PGA.

(H–K) Monoclonal and polyclonal patients do not differ in their PGA, irrespective of whether it is estimated by WGS (H) or microarray platforms (I). However, the BCR-free rate of monoclonal and polyclonal samples do differ when median dichotomized by PGA considering subclonal architecture for both WGS-estimates of PGA (J) and microarray-based PGA estimates (K). Statistical assessment in (J) and (K) used the log-rank test.
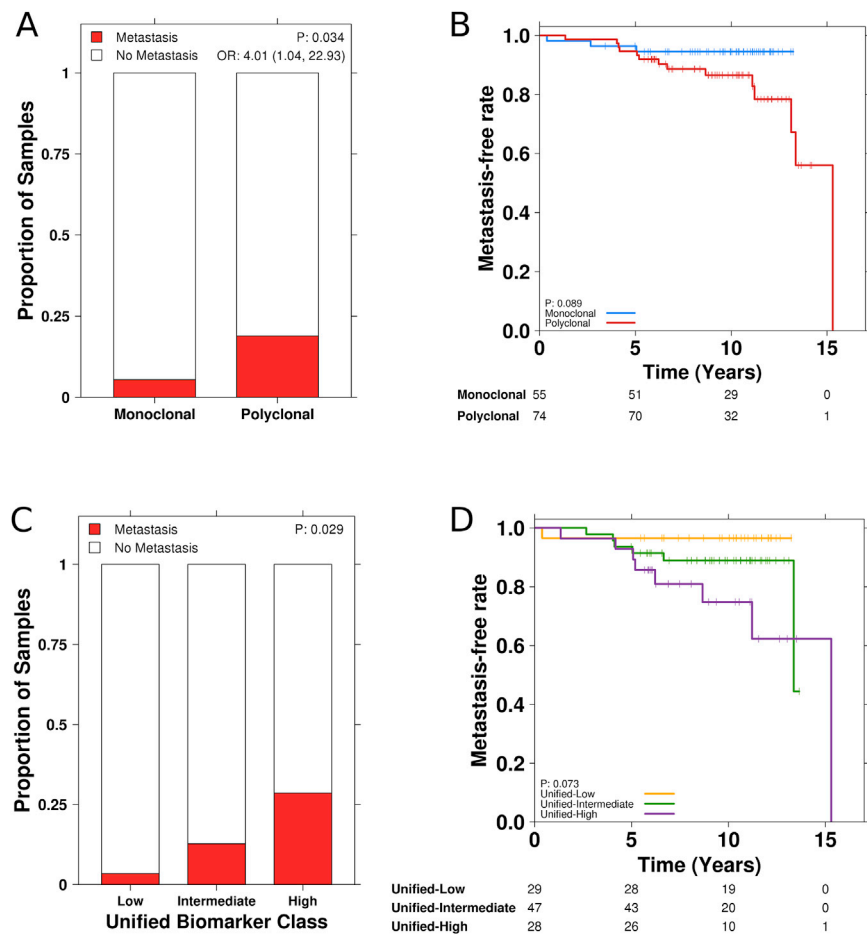
Figure S7. Clonality Associations with Tumor Metastasis, Related to Figure 7

(A) Patients with polyclonal tumors are enriched for metastasis.

(B) Further, they show a trend toward reduced metastasis-free rate, with statistical significance assessed using the log-rank test.

(C and D) The proportion of samples with a metastasis is significantly different between different classes of the unified biomarker (C), and this corresponds to trends toward inter-group differences in metastasis-free rate (D).